



Available online at www.sciencedirect.com

ScienceDirect

[Comput. Methods Appl. Mech. Engrg.](#)

**Computer methods
in applied
mechanics and
engineering**

www.elsevier.com/locate/cma

An effective and stabilised $(\mathbf{u} - \mathbf{p}_l)$ SPH framework for large deformation and failure analysis of saturated porous media

Yanjian Lian¹, Ha H. Bui^{1,2}®, Giang D. Nguyen², and Asadul Haque¹

¹Department of Civil Engineering, Monash University, Australia.

²School of Civil, Environmental & Mining Engineering, University of Adelaide, Australia.

ABSTRACT

Particle-based methods such as SPH have been proven to be powerful numerical tools for addressing challenges in solving coupled large deformation and failure of porous materials. In these applications, explicit time integration schemes are commonly adopted to integrate the coupled pore-water pressure equation. The Courant-Friedrichs-Lowy condition is required and imposes a strong restriction on the time increment, which is inversely proportional to the water bulk modulus, leading to a significant increase in the overall computational costs. This affects successful applications of SPH in solving field-scale fully coupled large deformation and failure of porous media. To address this problem, this study proposes a computationally efficient three-point integration (TPI) scheme that removes the influence of water bulk modulus from the pore-water pressure equation, enabling larger time increments for the time integration and hence saving computational costs for field-scale applications. Furthermore, a stabilised method is proposed to enable SPH to solve coupled flow-deformation of saturated porous media involving negative excess pore-water developments for the first time. The proposed SPH algorithm is verified against analytical and finite element solutions for small deformation ranges. Thereafter, it is applied to predict challenging problems involving large deformation and retrogressive failure of saturated porous materials, where contractive and dilative responses of porous materials can cause significant variations and instabilities in the development of excess pore-water pressure. The results suggest that the proposed SPH algorithm is stable and suitable for handling field-scale applications.

Keywords: SPH, three-point integration (TPI), large deformation, coupled flow-deformation analysis, retrogressive failure

© Corresponding author (Ha H Bui, Email: ha.bui@monash.edu)

1. Introduction

Developments of safety assessment and disaster prevention guidelines for engineering earth structures require a sound knowledge of coupled flow deformation analysis in saturated and unsaturated porous media and advanced computational tools that can foresee the worst-case scenarios should they happen (e.g., the impact of landslides or embankment failures should they occur). The Finite Element Method (FEM) is one of the most popular computational tools that are robust and could give satisfactory results for fully coupled problems involving small deformation analysis [1]. However, when dealing with large deformation and post-failure behaviour of materials, the standard FEM becomes less competitive due to the inherent severe mesh distortion issue [1–3]. Recent advanced mesh-based FEM methods have resulted in several powerful numerical methods capable of handling large deformation and post-failure behaviour of porous materials, such as the particle finite element method (PFEM) and material point method (MPM) [4–8]. An alternative approach to the FEM-based methods is the fully mesh-free methods, such as the Smoothed Particle Hydrodynamics (SPH) method, which offer an excellent capability to handle large deformation and post-failure problems.

As the eldest truly continuum-based mesh-free method, the SPH method was initially developed for astrophysical applications [9,10]. Since its successful applications in solving large deformation of elastoplastic materials [11], SPH has been widely used to solve a range of challenging geotechnical problems, including granular flows [12–15], slope failures [16–21], soil-structure interactions [22–25], desiccation cracking in soils [26,27] and rock fractures [28–30], to name a few. Besides, there exist two SPH approaches for solving coupled fluid-solid interaction problems, namely the multi-layer approach [1,31–33] and the single-layer scheme [3,34–39]. In the first approach, the multiphase porous media is represented by multiple layers of particles, each of which follows its governing equations. The governing equations of each phase are solved separately on their own set of Lagrangian SPH particles. In the latter approach, the porous media is represented by a single layer of Lagrangian SPH particles, each of which carries all field information. The fully coupled governing equations are then established and solved on a single set of SPH particles [34–37,39].

The single-layer approach for coupled flow-deformation analysis is computationally cheaper than the multi-layer scheme. However, several challenges still exist in terms of numerical stabilities or computational costs associated with this approach when used for large-scale applications. For example, in the earliest attempt to solve the fully coupled problems of fluid-saturated porous media using the single-layer SPH approach (i.e., fully explicit) based on the $(\mathbf{u} - p_l)$ formulation (\mathbf{u} stands for solid displacement and p_l indicates pore-water pressure) Bui

and Fukagawa [34] reported that strong fluctuation in the development of excess pore-water pressure was observed and attributed to large water bulk modulus and small water permeabilities. This instability in the pore-water pressure field is also a common issue in other Galerkin-based numerical methods (e.g., FEM and MPM) when applied to the coupled flow-deformation analysis of saturated porous media in the limit of undrained condition (i.e., very low permeability) with incompressible pore-fluid. It is often referred to as the inf-sup condition or Ladyženskaja-Babuška-Brezzi (LBB) condition in the literature [40,41], and advanced integration methods (e.g., direct α -method or the fractional-step method) are commonly used in FEM or MPM simulations [2,41–43] to address this issue. In this study, stabilised techniques are also proposed to address this challenge within the context of the SPH method.

Apart from the first attempt at solving the coupled flow-deformation problem in saturated media [34], Blanc and Pastor [44] also presented a single-layer SPH model ($\mathbf{u} - p_l$) adopting the so-called stress point approach and a fractional-time integration scheme based on the Runge–Kutta Taylor SPH algorithm, promising results were obtained when compared to analytical solutions. Recently, more attempts based on the single-layer SPH approach have been reported in the literature. For instance, Morikawa and Asai [38] presented a single-layer SPH approach based on the $(\mathbf{u} - \mathbf{w} - p_l)$ formulation (\mathbf{w} is the water flow velocity) to solve coupled flow-deformation of saturated soils, adopting an incompressible SPH (ISPH) approach to solve the pore-pressure equation (i.e., implicit) and achieved promising results, particularly for 1D consolidation problems compared to analytical solutions. Lian et al. [36,37] proposed an efficient single-layer SPH framework based on the $(\mathbf{u} - p_a - p_l)$ formulation (p_a is the pore air pressure) for describing the dynamics flows and fully coupled deformation of unsaturated porous media (i.e., fully explicit), which were fully validated against analytical solutions and experiments. Ma et al. [39] extended the single-layer SPH approach proposed by Lian et al. [36,37] to solve their five-phase mathematical model to describe a complex seepage-induced internal erosion and failure of porous media process and achieve promising results compared to both analytical solutions and experiments. Overall, the single-layer SPH approach has been proven to be a robust method to deal with field-scale and complex coupled problems of saturated and unsaturated porous media. However, existing fully explicit SPH solvers are restricted by the CFL condition, which imposes a strong constraint on the timestep increment, which is inversely proportional to the water bulk modulus [2,45,46], hence causing a significant increase in the overall computational costs. Therefore, an alternative time integrations scheme is still needed to improve its computational efficiency.

This paper aims to address the above limitation of the fully explicit SPH solver in solving the fully coupled problems of saturated porous media by proposing an efficient and stabilised SPH framework. The paper is organised as follows: first, the fully coupled two-phase SPH computational framework based on the $(\mathbf{u} - p_l)$ formulation for saturated porous media is briefly introduced. Thereafter, a three-point integration (TPI) scheme is proposed and verified by means of a range of 1D consolidation and 2D bearing capacity problems. Finally, the enhanced SPH framework is applied to predict the granular collapse of fully saturated soils and retrogressive failure problems to illustrate the capability of the model in the fully coupled flow-large deformation analysis.

2. Governing equations of the framework

2.1 Governing differential equations

In this study, the following assumptions are used in the derivation of the mathematic framework for the fully saturated porous medium:

- i. The saturated medium consists of a solid skeleton and a connected void filled with water.
- ii. The solid grain and the water phase are assumed to be incompressible.
- iii. The system is isothermal, and no mass exchange among phases.
- iv. Terzaghi's effective stress concept is assumed to be acceptable.

Based on the above assumptions, a brief introduction of the governing equations (i.e., $\mathbf{u} - p_l$ formulation) for fully coupled flow-deformation analysis is given in this section. The behaviour of saturated porous media is governed by the interaction between solid skeleton and pore-fluids, each of which is considered as a homogenised continuum that follows its governing equations, which take the forms of:

$$\bar{\rho}_\alpha \frac{d^\alpha \mathbf{v}_\alpha}{dt} = \nabla \cdot \bar{\boldsymbol{\sigma}}_\alpha + \bar{\rho}_\alpha \mathbf{b} - \sum \mathbf{R}^s \quad (1)$$

where $\bar{\rho}_\alpha = n_\alpha \rho_\alpha$ is the partial density of phase α ; \mathbf{b} is the body force vector; $\bar{\boldsymbol{\sigma}}_\alpha$ is the partial stress for each phase, which is given for solid and water phases as follows, respectively:

$$\begin{aligned} \bar{\boldsymbol{\sigma}}_s &= \boldsymbol{\sigma}' - (1 - n)p_l \mathbf{I} \\ \bar{\boldsymbol{\sigma}}_l &= -np_l \mathbf{I} \end{aligned} \quad (2)$$

where n is the porosity; \mathbf{I} is the second-order unity identity tensor; p_l the pore-water pressure; $\boldsymbol{\sigma}' = \boldsymbol{\sigma} + p_l \mathbf{I}$ is Terzaghi's effective Cauchy stress, which is valid for saturated porous media with incompressible solid grains; and $\boldsymbol{\sigma} = \bar{\boldsymbol{\sigma}}_s + \bar{\boldsymbol{\sigma}}_l$ is the total Cauchy stress tensor.

The drag force vector between fluid and solid phases \mathbf{R}^s in Eq. (1) takes the following form:

$$\mathbf{R}^s = \frac{n\rho_l g}{\mathbf{k}_\alpha} n \bar{\mathbf{w}}_{\alpha\beta} - p_l \nabla n \quad (3)$$

where \mathbf{k}_α denotes the second-order permeability tensor of the fluid phase α , which is a function of void ratio following the form of [37,47]:

$$\mathbf{k}_\alpha(e) = \mathbf{k}_{sat}^0 \exp\left(\frac{e - e_0}{C_k}\right) \quad (4)$$

where $\mathbf{k}_{sat}^0 = k_{sat} \mathbf{I}$ is the permeability tensor; e and e_0 are the current and initial void ratio, which can be linked to porosity change; C_k is the Kozeny-Carman coefficient; and ρ_l stands for the intrinsic mass density of water. The last term on the right-hand side in Eq. (3) is known as the Buoyancy force acting on the solid phase.

Substituting Eq. (3) into the momentum balance equation for the water phase, the following relative velocity between the solid and water phase in fully saturated soil can be obtained [36,37,46,47]:

$$\bar{\mathbf{w}}_{ls} = \frac{\mathbf{k}_l}{n\gamma_l} \left(-\nabla p_l + \rho_l \mathbf{b} - \rho_l \frac{d^s \mathbf{v}_s}{dt} \right) \quad (5)$$

The momentum equation for the entire mixture can be obtained by adding the momentum equation for each phase, and after neglecting the relative acceleration between solid and water, yielding [46]:

$$\frac{d^s \mathbf{v}_s}{dt} = \frac{1}{\rho_t} \nabla \cdot \boldsymbol{\sigma} + \mathbf{b} \quad (6)$$

where ρ_t is the total density.

Different from the double-layer SPH approach, where the motion of the mixture is achieved by solving each phase's momentum equation [1], in this single-layer SPH model, the motion of the mixture is achieved by solving Eq. (6). The behaviour of the water phase is described by the evolution of pore-water pressure as an additional variable to the solid particle. The governing equation for the pore-water pressure evolution can be derived from the mass balance equations. The general form of the mass balance equation for each phase in the mixture is given as:

$$\frac{d^\alpha \bar{\rho}_\alpha}{dt} + \bar{\rho}_\alpha \nabla \cdot \mathbf{v}_\alpha = 0 \quad (7)$$

By substituting the partial density of the solid phase into Eq. (7), the mass balance equation for the solid phase in terms of the time derivative of porosity can be obtained:

$$\frac{d^s n}{dt} = (1 - n) \nabla \cdot \mathbf{v}_s \quad (8)$$

It is noted that Eq. (8) is obtained by enforcing the incompressibility of the solid grain. Similarly, the following mass conservation equations for the water phase can be obtained by introducing the partial density in Eq. (7) as [36,37]:

$$\frac{n}{K_l} \frac{d^s p_l}{dt} + \nabla \cdot \mathbf{v}_s + \nabla \cdot (n \bar{\mathbf{w}}_{ls}) = 0 \quad (9)$$

where K_l stands for the fluid bulk modulus. By introducing Eq. (5) into Eq. (9), the general equations governing the seepage flow through deformable saturated porous media can be obtained as follows:

$$\frac{d^s p_l}{dt} = \frac{K_l}{n} \left\{ -\nabla \cdot \mathbf{v}_s + \frac{1}{\gamma_l} \nabla \cdot [\mathbf{k}_l \nabla (p_l + \rho_l g z)] + \frac{1}{g} \nabla \cdot \left(\mathbf{k}_l \frac{d^s \mathbf{v}_s}{dt} \right) \right\} \quad (10)$$

where z is the elevation, which becomes zero if the gravity is neglected.

Equation (10) governs the evolution of pore water pressure in the deformable saturated porous media, and together with Eqs. (6) and (8), they form three fundamental governing equations, also known as the $(\mathbf{u} - p_l)$ formulation, for the coupled flow-deformation framework of saturated porous media. Besides the $(\mathbf{u} - p_l)$ formulation, another form of formulation, namely $(\mathbf{u} - \mathbf{w})$, can also be obtained using the same derivation process by neglecting the convective term or the relative acceleration term. Thus, $(\mathbf{u} - \mathbf{w})$ and $(\mathbf{u} - p_l)$ formulations share similar features and are more appropriate for low-frequency dynamics problems [46,48,49], which is the focus of this study. For high-frequency problems, such as earthquake-induced failure problems, the $(\mathbf{u} - \mathbf{w} - p_l)$ formulation was often recommended [46].

2.2 Constitutive equation

A constitutive relation is required to describe the soil's deformation behaviour or to compute the effective stress in the above governing equations. Detailed descriptions of how to implement a material constitutive model in SPH can be found in Bui and Nguyen [3]. In this study, only essential formulations are summarised to provide background for our SPH development. The effective stress increment is updated using the following equation:

$$d\boldsymbol{\sigma}^J = \mathbf{D}^e (d\boldsymbol{\epsilon} - d\boldsymbol{\epsilon}^p) = d\boldsymbol{\sigma}' + d\boldsymbol{\omega} \cdot \boldsymbol{\sigma}' - \boldsymbol{\sigma}' \cdot d\boldsymbol{\omega} \quad (11)$$

where \mathbf{D}^e is the elastic stiffness matrix; $d\boldsymbol{\sigma}^J$ is the increment of the Zaremba-Jaumann stress tensor of the effective Cauchy stress tensor according to the updated Lagrangian approach using small strains; $d\boldsymbol{\omega}$ stands for the spin increment tensor; and $d\boldsymbol{\epsilon}^p$ is the plastic strain increment, which takes the form of:

$$d\boldsymbol{\epsilon}^p = d\lambda \frac{\partial g_0}{\partial \boldsymbol{\sigma}'} \quad (12)$$

where g_0 is the plastic potential function; and $d\lambda$ is the non-negative plastic multiplier, which can be computed using the semi-implicit stress return mapping algorithm given by [3] :

$$d\lambda = \frac{f}{\frac{\partial f}{\partial \boldsymbol{\sigma}'} : \mathbf{D}^e : \frac{\partial g_0}{\partial \boldsymbol{\sigma}'} + \frac{\partial f}{\partial \kappa} \sqrt{\frac{2}{3} \frac{\partial g_0}{\partial \mathbf{s}} : \frac{\partial g_0}{\partial \mathbf{s}}}} \quad (13)$$

with f being the trial value of a plastic-yielding function caused by an elastic stress increment, assuming no plastic deformation. The Drucker Prager (DP) strain-softening constitutive model [3,37,50,51] is adopted in this study. The yielding and plastic potential functions of this model take the following forms, respectively:

$$f = \xi_\phi I_1 + \sqrt{J_2} - \kappa_c \quad (14)$$

$$g_0 = \xi_\psi I_1 + \sqrt{J_2} \quad (15)$$

where I_1 and J_2 are the first and second invariants of the effective stress tensor; ξ_ϕ and κ_c are DP constitutive parameters related to the friction (ϕ) and cohesion (c) of the soil. Under the plane strain condition, these parameters are defined by:

$$\xi_\phi = \frac{\tan\phi}{\sqrt{9+12\tan\phi^2}} \quad \kappa_c = \frac{3c}{\sqrt{9+12\tan\phi^2}} \quad (16)$$

Finally, the following softening laws are adopted to replicate the critical state behaviour of the soil subjected to large shear deformation [3,37,50,51]:

$$\phi = \phi_r + (\phi_p - \phi_r) \exp(-\eta \varepsilon_p^{eq}) \quad (17)$$

$$c = c_r + (c_p - c_r) \exp(-\eta \varepsilon_p^{eq}) \quad (18)$$

$$\psi = \psi_0 \exp(-s_f \varepsilon_p^{eq}) \quad (19)$$

where the subscripts p and r denote the peak and residual strengths of the material, respectively; η is the softening coefficient controlling the rate of shear strength degradation with the plastic strain of the material; ε_p^{eq} is the accumulated equivalent plastic strain; ψ is the dilation angle; ψ_0 is the initial dilation angle; and s_f is a constant controlling the rate of dilatancy reduction.

3. SPH discretisation for the governing equations

3.1 A brief overview of SPH

In SPH, the computation domain is discretised into a finite number of particles, with each particle carrying field quantity, including mass, density, velocity and pressure [11]. These variables and their gradients at a given particle location are then computed by means of an integral process that uses the information from its surrounding particles by a kernel function. Let us first consider an arbitrary field quantity function $f(\mathbf{x})$ at any point \mathbf{x} in the computational domain, the integral representation of this function can be written as follows:

$$\langle f(\mathbf{x}_i) \rangle = \sum_{j=1}^N V_j f(\mathbf{x}_j) W(\mathbf{x}_i - \mathbf{x}_j, h_{sml}) \quad (20)$$

where the angle bracket $\langle \rangle$ indicates the kernel approximation operator; V_j is the volume occupied by particle j ; $W(\mathbf{x}_i - \mathbf{x}_j, h_{sml})$ is a symmetric smoothed (or kernel) function, which has a characteristic length h_{sml} defining an effective domain Ω of the smoothing function. Among several popular kernel functions reported in the literature [3,52], the cubic spline kernel function is adopted in this paper, which takes the following forms:

$$W(q, h_{sml}) = \alpha_d \begin{cases} \frac{2}{3} - q^2 + \frac{1}{3}q^3 & 0 \leq q < 1 \\ \frac{1}{6}(2-q)^3 & 1 \leq q < 2 \\ 0 & q > 2 \end{cases} \quad (21)$$

where α_d is the dimensional normalising factor defined by $\alpha_d = [1/h, 15/7\pi h^2, 3/2\pi h^3]$ for one, two and three-dimensions, respectively; and q is the normalised distance defined as $q = |\mathbf{x}_i - \mathbf{x}_j|/h_{sml}$ where $h_{sml} = 1.2dx$ with dx being the initial distance between particles. The SPH approximation for both the first-order and second-order gradient of function $f(\mathbf{x}_i)$ can be obtained by applying the Taylor series expansion of function $f(\mathbf{x}_j)$ about \mathbf{x}_i , and there exist several formulations reported in the literature [3,36]. In this work, the following corrected SPH formulation for the first-order gradient of $f(\mathbf{x}_i)$ is adopted [53,54]:

$$\nabla_i^m f(\mathbf{x}_i) = \sum_{j=1}^N V_j [f(\mathbf{x}_j) - f(\mathbf{x}_i)] \hat{\nabla}_i^m W_{ij} \quad (22)$$

where $\hat{\nabla}_i^m W_{ij} = L_{ij}^{mn} \nabla_i^n W_{ij}$ with $L_{ij}^{mn} = [\sum_{j=1}^N V_j (x_j - x_i)^m \nabla_i^n W_{ij}]^{-1}$ being the normalised matrix, and m and n indicate coordinate direction with repeated indices implying summation. Similarly, several robust SPH approximations exist for the second-order derivatives in the literature [3,36,55,56]. In this work, the general SPH approximation for the second-order

derivatives, recently proposed by the authors and achieved excellent accuracy for highly disordered particle systems, is adopted and takes the forms of [36]:

$$\frac{\partial^2 f_i}{\partial x^m \partial x^n} = \sum_{j=1}^N V_j (f_j - f_i) \mathcal{D}^{mn} \tilde{F}_{ij} - \frac{\partial f_i}{\partial r^{m'}} \sum_{j=1}^N V_j r_{ji}^{m'} \mathcal{D}^{mn} \tilde{F}_{ij} \quad (23)$$

where $\mathcal{D}^{mn} = 4 \frac{r_{ji}^m r_{ji}^n}{|\mathbf{r}_{ji}|^2} - \delta^{mn}$ with δ^{mn} being the Kronecker delta function; and $\tilde{F}_{ij} = \frac{r_{ji}^m}{|\mathbf{r}_{ji}|^2}$.

$\hat{\nabla}_i^m W_{ij}$ is the scalar part of the normalised kernel gradient, with $\mathbf{r}_{ji} = \mathbf{x}_j - \mathbf{x}_i$ being the distance vector, and $\partial f / \partial r^{m'}$ is the first-order spatial gradient calculated from Eq. (22). It is noted that Eq. (23) shares a similar form to that proposed by Español & Revenga (2003) [56], except the last term on the right-hand side of the equation, which helps to remove approximation errors caused by particle distortion [36]. In this work, Eqs. (20), and (22)-(23) are adopted to discrete the governing equation for the coupled seepage-deformation framework, which is given in the next section.

3.2 SPH discretisation of the governing equations

The change of porosity determined by Eq. (8) can now be converted into the SPH approximation form. This can be achieved by applying Eq. (22) to the divergence term in Eq. (8), leading to the following SPH approximation for the porosity:

$$\frac{dn_i}{dt} = \sum_{j=1}^N V_j (1 - n_j) \mathbf{v}_{ji}^s \hat{\nabla}_i W_{ij} \quad (24)$$

where \mathbf{v}_{ji}^s is the velocity difference between two particles. Once the porosity of the soil skeleton is determined from Eq. (24), the variation of saturated permeability and the specific moisture term can be updated. Similarly, the SPH approximation for the time derivative of pore-water pressure can be obtained:

$$\begin{aligned} \frac{dp_l}{dt}_i = & \frac{K_l}{n} \left\{ \frac{1}{\gamma_l} \sum_{j=1}^N V_j \bar{k}_{mn}^{ji} p_l^{ji} \mathcal{D}^{mn} \tilde{F}_{ij} + \sum_{j=1}^N V_j \bar{k}_{mn}^{ji} z_{ji} \mathcal{D}^{mn} \tilde{F}_{ij} \right. \\ & - k_i^{mn} \frac{\partial p_l}{\partial r^{m'}} \sum_{j=1}^N V_j r_{ji}^{m'} \mathcal{D}^{mn} \tilde{F}_{ij} - \sum_{j=1}^N V_j \mathbf{v}_{ji}^s \hat{\nabla}_i W_{ij} \\ & \left. + \frac{1}{g} \sum_{j=1}^N V_j \bar{k}_{mn}^{ji} \left(\frac{d\mathbf{v}_{ji}^s}{dt} \right) \hat{\nabla}_i W_{ij} \right\} \end{aligned} \quad (25)$$

where $\bar{k}_{mn}^{ji} = (k_{mn}^i + k_{mn}^j)/2$ is the arithmetically mean value of water permeability; $p_l^{ji} = (p_l^j - p_l^i)$ is the pressure difference; z_{ji} in the second term of Eq. (25) is the elevation difference between particles, which could vanish if gravity is not considered.

The motion of the solid particle is described by the momentum equation of the whole mixture in terms of total stress, i.e., Eq. (6), which is given as follows:

$$\left(\frac{d\mathbf{v}_s}{dt}\right)_i = \sum_{j=1}^N V_j \left(\frac{\boldsymbol{\sigma}_i + \boldsymbol{\sigma}_j}{\rho_i^t} + \mathbf{C}_{ij} \right) \nabla_i W_{ij} + \mathbf{b} \quad (26)$$

where ρ^t is the total density of particle i , which varies over time with the degree of saturation; and \mathbf{C}_{ij} is a stabilisation term consisting of the artificial viscosity and artificial stress commonly adopted in SPH to remove stress fluctuation and tensile instability, respectively [11,14,18,57,58]. In this paper, the same formulations and recommended parameters for the stabilisation term previously reported in [11,18] for geomechanics applications are adopted, except that the sound speed of soil required for the artificial viscosity is computed following [18].

3.3 SPH time discretisation

The Leap-Frog (LF) algorithm is usually used to integrate the SPH approximation equations developed in the preceding section. In this approach, the state variables (Υ), including porosity (n), water pressure (p_l), effective stress ($\boldsymbol{\sigma}$) and velocity (\mathbf{v}_s), are updated at the mid-step in time, while the displacement vector is updated at the full-time step as follows:

$$\begin{aligned} \Upsilon_{t+\Delta t/2} &= \Upsilon_{t-\Delta t/2} + \Delta t \left(\frac{d\Upsilon}{dt} \right)_t \\ \mathbf{x}_{t+\Delta t}^s &= \mathbf{x}_t^s + \Delta t \cdot (\mathbf{v}_s^s)_{t+\Delta t/2} \end{aligned} \quad (27)$$

The stability of the LF time integration scheme is maintained by the Courant-Friedrichs-Lowy (CFL) condition. The commonly-used CFL criterion to ensure the stability of the fully explicit time integration scheme for the fully coupled analysis of saturated porous media is [2,42,46] :

$$\Delta t_s \leq \frac{l}{c_{sp}} \quad (28)$$

where l is the length scale, which can be taken as the initial distance between SPH particles;

and c_{sp} is the sound speed defined as $c_{sp} = \sqrt{\left(\frac{K_l}{n} + \frac{4}{3}G\right)/(n\rho_l + n_s\rho_s)}$.

The time step size given in Eq. (28) is inversely proportional to the fluid bulk modulus (K_l); thus it is often very small if an actual value of fluid bulk modulus is adopted, causing a

significant increase in the overall computational costs. This issue can be addressed using the proposed TPI algorithm, which will be described in the next section.

3.4 Three-point integration (TPI) scheme

To address the issue associated with the large water bulk modulus and enable a larger time step size, let us first recast the seepage flow governing equation, i.e., Eq. (10), into the following forms:

$$\frac{n}{K_l} \frac{d^s p_l}{dt} + \nabla \cdot \mathbf{v}_s - \frac{1}{\gamma_l} \nabla \cdot [\mathbf{k}_l \nabla (p_l + \rho_l g z)] - \frac{1}{g} \nabla \cdot \left(\mathbf{k}_l \frac{d^s \mathbf{v}_s}{dt} \right) = 0 \quad (29)$$

Next, to remove the influence of the water bulk modulus from the above equation, one could enforce the incompressibility condition to the water phase, leading to the vanishing of the specific storage term $C_l = n/K_l$. Accordingly, the governing equation for seepage flow in deformable porous media is reduced to:

$$\nabla \cdot \mathbf{v}_s - \frac{1}{\gamma_l} \nabla \cdot [\mathbf{k}_l \nabla (p_l + \gamma_l z)] - \frac{1}{g} \nabla \cdot \left(\mathbf{k}_l \frac{d^s \mathbf{v}_s}{dt} \right) = 0 \quad (30)$$

The key question now is how to find the solution for the pore-water pressure p_l in Eq. (30), and this can be achieved in several ways. By expanding the second derivative term, Eq. (30) can be rewritten as follows:

$$\nabla \cdot (\mathbf{k}_l \nabla p_l^{t+1})_i = \gamma_l (\nabla \cdot \mathbf{v}_s)_i - \gamma_l \nabla \cdot [\mathbf{k}_l \nabla (z)]_i - \rho_l \nabla \cdot \left(\mathbf{k}_l \frac{d^s \mathbf{v}_s}{dt} \right)_i \quad (31)$$

The second derivative of the pore-water pressure in Eq. (31) can be discretised using the recently proposed SPH approximation (23) [36], which leads to:

$$\nabla \cdot (\mathbf{k}_l \nabla p_l^{t+1})_i = \left[\sum_{j=1}^N (p_l_j^{t+1} - p_l_i^{t+1}) A_{ij} - E_i \right] \quad (32)$$

where the operator A_{ij} and the error source term E_i are given as follows:

$$A_{ij} = V_j \bar{k}_{mn}^{ji} \mathcal{D}^{mn} \tilde{F}_{ij} \quad (33)$$

$$E_i = k_i^{mn} \frac{\partial p_{l_i}}{\partial r^{m'}} \sum_{j=1}^N V_j r_{ji}^{m'} \mathcal{D}^{mn} \tilde{F}_{ij}$$

where $\bar{k}_{mn}^{ji} = (k_{mn}^i + k_{mn}^j)/2$ is the arithmetically mean value of water permeability. By substituting the above SPH approximation into Eq. (31), the following equation can be obtained:

$$\sum_{j=1}^N (p_{l_j}^{t+1} - p_{l_i}^{t+1}) A_{ij} = \gamma_l (\nabla \cdot \mathbf{v}_s)_i - \gamma_l \nabla \cdot [\mathbf{k}_l \nabla (z)]_i - \rho_l \nabla \cdot \left(\mathbf{k}_l \frac{d^s \mathbf{v}_s}{dt} \right)_i + E_i \quad (34)$$

The above equation was written in the form of a linear system equation of unknown variables being p_l^{t+1} . This linear system equation can be solved using a precondition conjugate gradient iterative method [59]. However, this method requires very high memory storage to store the particle matrix and appropriate free-surface pressure boundary conditions; thus, it is limited to a small number of particles. Alternatively, a more straightforward approach is used in this study to solve the above pore-water pressure equations. This can be achieved by further expanding Eq. (34), giving:

$$p_{l_i}^{t+1} = \frac{B_{ij} + \sum_{j=1}^N A_{ij} p_{l_j}^{t+1}}{\sum_{j=1}^N A_{ij}} \quad (35)$$

where B_{ij} is the source term for $p_{l_i}^{t+1}$ defined as follows:

$$B_{ij} = -\gamma_l (\nabla \cdot \mathbf{v}_s)_i + \gamma_l \nabla \cdot [\mathbf{k}_l \nabla (z)]_i + \rho_l \nabla \cdot \left(\mathbf{k}_l \frac{d^s \mathbf{v}_s}{dt} \right)_i - E_i \quad (36)$$

For a small-time increment, the unknown p_l^{t+1} on the right-hand side of Eq. (35) can be approximately assumed equal to p_l^t from the previous time step, i.e., $p_l^{t+1} \approx p_l^t$, [1,59–61], leading to:

$$p_{l_i}^{t+1} = \frac{B_{ij} + \sum_{j=1}^N A_{ij} p_{l_j}^t}{\sum_{j=1}^N A_{ij}} \quad (37)$$

Both two terms on the right-hand side of Eq. (37) are known at instant t , and thus the pressure p_l^{t+1} at time $t + 1$ can be explicitly calculated. Equation (37) removes the pore-water pressure dependence from the water bulk modulus, thus enabling a larger time step size for the time integration of the pore pressure equation. However, some care still need to be taken to obtain a stable and accurate solution. This is because Eq. (37) makes use of $p_{l_j}^{t+1} \approx p_{l_j}^t$, and thus

could only produce accurate results for a small time increment [1,59–61]. Hence, this assumption might lead to accumulated errors in the numerical solution when a large time increment is used [61]. To mitigate this issue, the above pore-pressure update equation can be revised as follows:

$$p_{l_i}^{t+1} = \frac{B_{ij} + \sum_{j=1}^N A_{ij} p_{l_j}^{t+\alpha}}{\sum_{j=1}^N A_{ij}} \quad (38)$$

where $p_{l_j}^{t+\alpha}$ is an “intermediate” pressure, which can be evaluated using the following linear approximation:

$$p_{l_j}^{t+\alpha} = p_{l_j}^t + \alpha(p_{l_j}^t - p_{l_j}^{t-1}) \quad (39)$$

with α being a corrected coefficient, whose value should be in a range of 0 – 1. For $\alpha = 0$, the proposed formulation (38) for the pore-pressure update returns to the fully explicit form (37), whereas for $\alpha = 1$, it replicates the fully implicit form (35), which is unconditionally stable [62]. To avoid these two limiting cases, the value of $p_{l_j}^{t+\alpha}$ needs to be evaluated and the proposed formulation (39) represents the key concept of the three-point integration (TPI) scheme, where the value of $p_{l_j}^{t+\alpha}$ at time $(t + \alpha)$ is estimated from the previously known pore-pressures at times $(t - 1)$ and t . The accuracy of the proposed TPI algorithm depends on the selection of α , whose optimal value also depends on the timestep size adopted in the simulation. Our numerical investigation suggests that $\alpha = 0.5$ could provide reasonably accurate and stable solutions for the pore-water pressure, and this value of α is adopted in all applications in this study.

Compared to the fully explicit time integration for the pore-fluid pressure equation reported in [35] or [36], the proposed TPI scheme removes the dependence of the pore-fluid pressure equation from the fluid bulk modulus, thus offering a more computationally efficient approach with a larger timestep size for the numerical solution. However, because the value of $p_{l_j}^{t+\alpha}$ is not directly evaluated at time $(t + \alpha)$, the proposed TPI approach only approximates the fully implicit solution, and hence it is not unconditionally stable and its stability is still constrained by a specific condition. In this study, the following criterion for the timestep is adopted:

$$\Delta t \leq \min(\Delta t_s, R\Delta t_l) \quad (40)$$

where Δt_s is the mechanical timestep for the solid phase; Δt_l is the critical timestep for the fluid phase defined in the standard explicit SPH formulation, and R is the amplifier coefficient

offered by the proposed TPI scheme, and its magnitude is proportional to permeability for the same particle resolution. The larger permeability is, the higher value of R can be adopted.

For the solid phase, the timestep is restricted by:

$$\Delta t_s \leq C_{CFL}^s \frac{h_{sml}}{c_{sp}} \quad (41)$$

where C_{CFL}^s is a constant, which is taken to be 0.1 throughout this paper; $c_{sp} = \sqrt{E_s/\rho_s}$ is the speed of sound in the solid phase with E_s being Young's modulus of the solid material; and h_{sml} is the smoothing length.

On the other hand, for the fluid phase in saturated soils, the timestep is given by [36]:

$$\Delta t_l \leq C_{CFL}^l \frac{n\gamma_l h_{sml}^2}{K_l k^{sat}} \quad (42)$$

Unlike other criteria reported in the literature [1,39], the critical timestep is designed to fulfil the CFL conditions for both the solid and fluid phases in this study. The hydraulic time step is inversely proportional to the product of fluid bulk modulus (K_l) and saturated permeability of soil (k^{sat}). As a result, a larger critical hydraulic timestep size can be adopted in applications with small permeabilities. However, the critical timestep required for the solid phase is restricted by the CFL condition (41), which usually results in a relatively small timestep. Thus, the mechanical time step will serve as the cap value to ensure the stability of the entire integration process. In this scenario, the fully explicit time integration scheme is still recommended for applications with very small permeabilities. On the other hand, for highly-permeable soils, the critical timestep will be dominated by the hydraulic one, which is always insignificantly small. In this scenario, the proposed method can overcome the timestep restriction by the fluid phase, thus enabling a larger timestep size to be used in the simulation and serving as an alternative time integration scheme to save computational costs.

Figure 1 shows the SPH computational procedure for solving coupled flow-deformation problems using the proposed TPI algorithms. Compared to the fully explicit time integration scheme, we only modify how the pore-water pressure is calculated using the newly proposed formulation. All other variables are still updated following the standard LF integration algorithm. The advantage of the proposed time integration is that it partially eliminates the CFL constraint for the fluid phase, enabling a larger time step to be used for applications involving relatively high hydraulic permeabilities. Verification examples will be demonstrated in Sections 4.1 and 4.2.

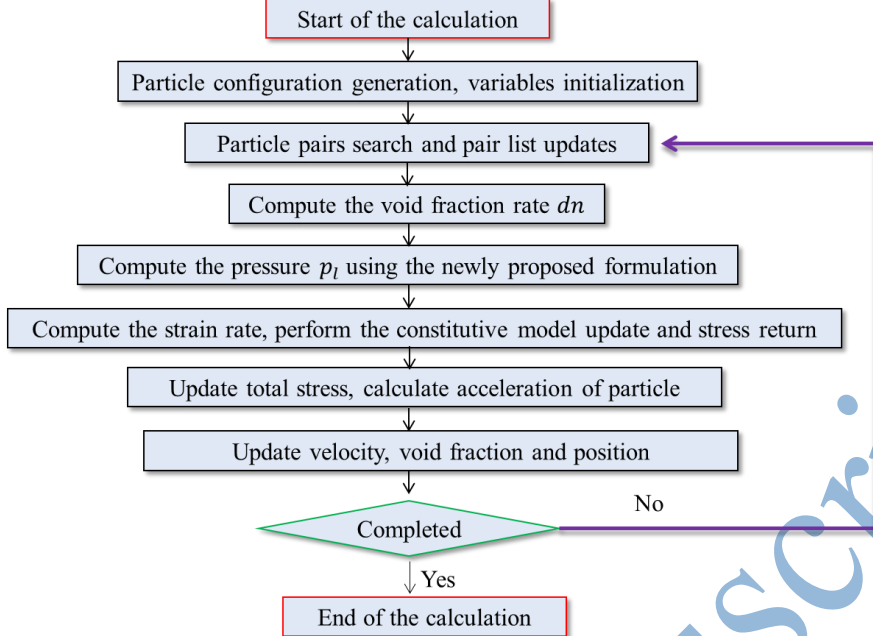


Fig. 1 SPH computational procedure for fully coupled flow-deformation analysis

3.5 Stabilised procedure

3.5.1 Global viscosity damping

In the current SPH framework for fully coupled flow-deformation problems, the motion of particles is governed by their fully dynamic momentum equation, i.e., Eq. (6). As a result, SPH particles may be subjected to free vibration due to inertial force or sudden external loads. Although the artificial viscosity is often incorporated in SPH simulations to smear out the shock, i.e., Eq. (26), thus acting as viscous damping in the momentum equation, it is insufficient to mitigate large fluctuations caused by sudden applied external loads in non-dissipative materials (or elastic materials). To remove this oscillation in non-dissipative materials to obtain smooth and accurate stress/pressure fields, the widely used stabilised procedure, namely the global viscous damping [14,63], is applied in this study. This global damping force is related to the particle velocity but acts in the opposite direction to the particle itself and takes the following forms [14,63]:

$$\mathbf{F}_d = -c_d \cdot \mathbf{v}_s \quad (43)$$

where c_d is the damping coefficient, determined from solid properties following the approach proposed by Bui et al. (2013) [63] as follows:

$$c_d = \eta_d \sqrt{E_s / (\rho_s h_{sml}^2)} \quad (44)$$

where η_d is a non-dimensional damping coefficient, of which the value is range from 0.02 to 0.1 as recommended by Bui et al. (2013) [63]. After adding the global viscous damping force, the final momentum equation is given as follows:

$$\left(\frac{d\mathbf{v}_s}{dt} \right)_i = \sum_{j=1}^N V_j \left(\frac{\boldsymbol{\sigma}_i + \boldsymbol{\sigma}_j}{\rho_i^t} + \mathbf{C}_{ij} \right) \nabla_i W_{ij} + \mathbf{F}_d + \mathbf{b} \quad (45)$$

It is noted that the global viscosity damping force is only applied to non-dissipative or elastic materials. Additional stabilisation methods are required for elastoplastic materials undergoing large deformation, and these will be discussed in the following sections.

3.5.2 Stabilisation of pore-water pressure

Non-physical spatial oscillation in the fluid pressure field is often reported when solving the fully coupled flow-deformation governing equations. This well-known instability issue is commonly found in continuum methods, including FEM and other mesh-based methods, and is mainly attributed to the stiff response of the material, i.e., incompressible or nearly incompressible fluid, causing pore-water pressure fluctuation [42,46]. In the proposed SPH framework, this pressure noise issue is only found in the coupled flow-deformation analysis of low-permeable soils, where the fluid is treated as an incompressible or nearly incompressible fluid. To overcome this issue, the moving least square (MLS) stress regulations technique proposed in [14] can be used to smooth out the noise in the pore water pressure field. In this study, a simpler and straightforward approach that makes use of the Shepard regularisation technique is adopted:

$$p_l^i = \frac{\sum_{j=1}^N V_j W_{ij} p_l^j}{\sum_{j=1}^N V_j W_{ij}} \quad (46)$$

Equation (46) is applied to each particle after every m computational cycle, which may vary from different applications[14,39]. In this study $m = 20\sim40$ is adopted, and it is only applied to coupled flow-deformation problems involving low permeable materials undergoing large deformation, i.e., demonstration cases in Section 4.5.

3.5.3 Negative pore water pressure stabilisation

The newly proposed integration scheme captures well the pore-water pressure evolution in the fully saturated soils undergoing non-volumetric deformation (i.e., zero dilatancies) or plastic

contraction. However, it becomes challenging when dealing with dilative soils, where the negative excess pore-water pressure develops due to plastic dilations. This is because Eq. (38) can overestimate the increased negative excess pore-water pressure when the soil is subjected to shearing dilation, a specific response of porous granular materials. This overestimated negative excess pore pressure could further lead to tensile stress in fully saturated soils, which facilitates the well-known tensile instability problems in SPH. To tackle this issue, a negative pore-water pressure cut-off could be applied by setting the pore-water pressure to zero once the negative pore-water pressure takes place. The disadvantage of this approach is that the proposed computational model is no longer capable of capturing the development of negative excess pore-water pressure and thus fails to capture the essential physics of saturated porous granular materials. Alternatively, another set of a formulation can be used to specially treat the negative excess pore pressure associated with plastic dilation and is given as follow:

$$p_{l_i}^{t+1} = \begin{cases} \frac{B_{ij} + \sum_{j=1}^N A_{ij} p_{l_j}^{t+\alpha}}{\sum_{j=1}^N A_{ij}} & p_l^t > 0 \\ \frac{B_{ij} + \sum_{j=1}^N A_{ij} p_{l_j}^{t+\alpha} + \beta p_{l_i}^{t+\alpha}/\Delta t}{\sum_{j=1}^N A_{ij} + \beta/\Delta t} & p_l^t < 0 \end{cases} \quad (47)$$

where β is the stabilisation coefficient governing the increasing rate of the negative pore-water pressure associated with plastic volumetric dilation, and its value can be calibrated from the standard triaxial tests, where the negative excess pore-water pressure caused by shear-induced dilation can be measured and compared with the numerical solutions. In this study, $\beta = 0.04$ is adopted in all simulation. Equation (47) slows down the increase rate in the negative pore-water pressure as the soil undergoes plastic dilation, thus providing sufficient time for SPH particles to respond to the development of negative excess pore-water pressure and achieving stabilised solutions. It is noted that Eq. (47) should only be adopted when plastic deformation is considered in the soil.

4. Verifications and applications

4.1 Verification through 1D Terzaghi's consolidation problem

The proposed integration scheme is first verified against the 1D Terzaghi's consolidation problem by comparing the predicted results with the theoretical solutions and those of the fully explicit LF algorithm previously reported by the authors [37]. Thereafter, the simulation is

repeated by increasing the time increment to demonstrate the performance of the proposed time integration scheme.

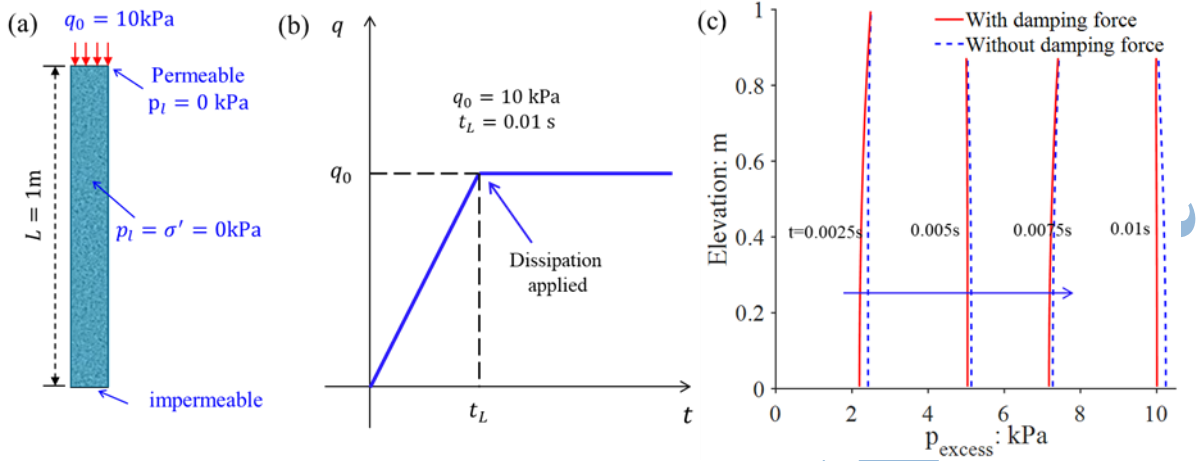


Fig. 2 SPH simulation of 1D consolidation (a) Geometry and boundary conditions; (b) the surcharge loading curve; (c) excess pore-water pressure built-up.

In this test, a fully saturated soil column, previously reported in [37] as shown in Fig. (2a), is modelled by 1000 particles with an initial particle spacing of 0.01m. The material is considered isotropic linear elastic with the following properties: Young's modulus of solid $E = 20 \text{ MPa}$, Poisson's ratio $\nu = 0.33$, void fraction $n = 0.4$, fluid bulk modulus $K_l = 1 \text{ GPa}$ and density $\rho_s = 2000 \text{ kg/m}^3$. The water density $\rho_l = 1000 \text{ kg/m}^3$, and the saturated permeability $k_{sat} = 2 \times 10^{-4} \text{ m/s}$, which remains unchanged in the simulation. The soil column is initialised with zero pore-water pressure and zero effective stress, and the gravity is also disregarded in this case. Then, a ramp load with a magnitude of 10 kPa is applied to the soil column within $t_L = 0.01\text{s}$ (see Fig. (2b)). During this loading stage, all boundaries are kept impervious so that the excess pore water pressure can build up. After that, a zero pore pressure is assigned to the soil column surface to trigger the pore-pressure dissipation process. No pore-pressure regularisation technique is applied in this case.

The suitability of the global damping stabilisation technique is first verified. Figure 2(c) shows the evolution of the excess pore-water pressure during the loading stage. It can be seen that the model overly predicts the excess pore-water pressure when the global damping force is not considered. However, after being adopted in the simulation, the global damping technique ($\eta_d = 0.02$) helped achieve the desirable excess pore-water pressure, equal to the surcharge loading on the upper surface.

The proposed integration scheme is then verified by comparing the consolidation results with those obtained by the fully explicit integration method reported in [37], as shown in Figure 3. The timestep is set to $\Delta t = 2.88 \times 10^{-7} s$, which is the same with [37] defined from the condition (42). It is seen that both integration schemes yield the same results, which agree well with the analytical solutions for both the excess pore-pressure and deformation, as shown in Figure 3.

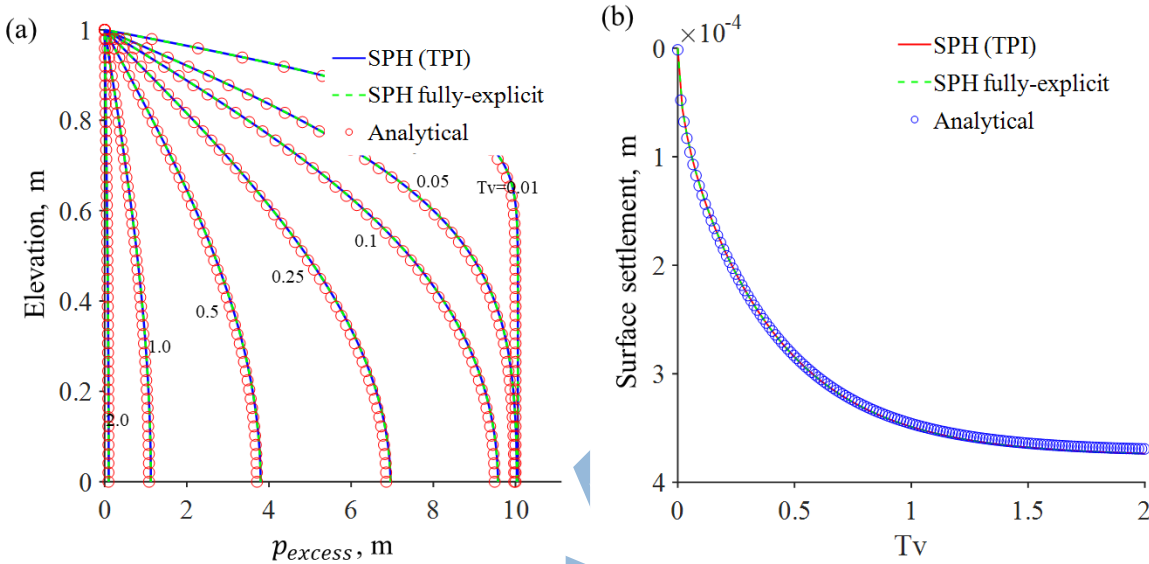


Fig. 3 SPH simulation of 1D consolidation with $\Delta t = 2.88 \times 10^{-7} s$: (a) The evolution of the excess pore-water pressure for different time intervals; (b) The evolution of the surface settlement

The 1D consolidation problem is then re-analysed by increasing the timestep size to demonstrate the capability of the proposed TPI time integration technique in saving computational costs. The timestep size is first increased by $R = 17$ times to $\Delta t = 5 \times 10^{-6} s$, and all other conditions are kept the same. It is worth noting that the fully explicit time integration scheme [37] could not handle the problem with such a significant timestep size since it violates the CFL condition (42) for solving the flow phase. Three simulations using Eq. (37) and Eq. (38) with different values of α (i.e., $\alpha = 0.0, 0.5$ and 0.7) are conducted for the dissipation stage, and the predicted results are shown in Figure 4(a). The solution predicted by Eq. (37), corresponding to coefficient $\alpha = 0$, introduced noticeable errors at the later stage of the consolidation process, which indicates that the assumption of $p_{l_j}^{t+1} \approx p_{l_j}^t$ introduced errors to the numerical solutions when the timestep size increased by 17 times. On the contrary, the proposed TPI scheme Eq. (38) produces a well-matched result with the analytical solutions for

both $\alpha = 0.5$ and 0.7 . In addition to the excess pore-water pressure, the effective stress is also in good agreement with the theoretical solution, as shown in Figure 5.

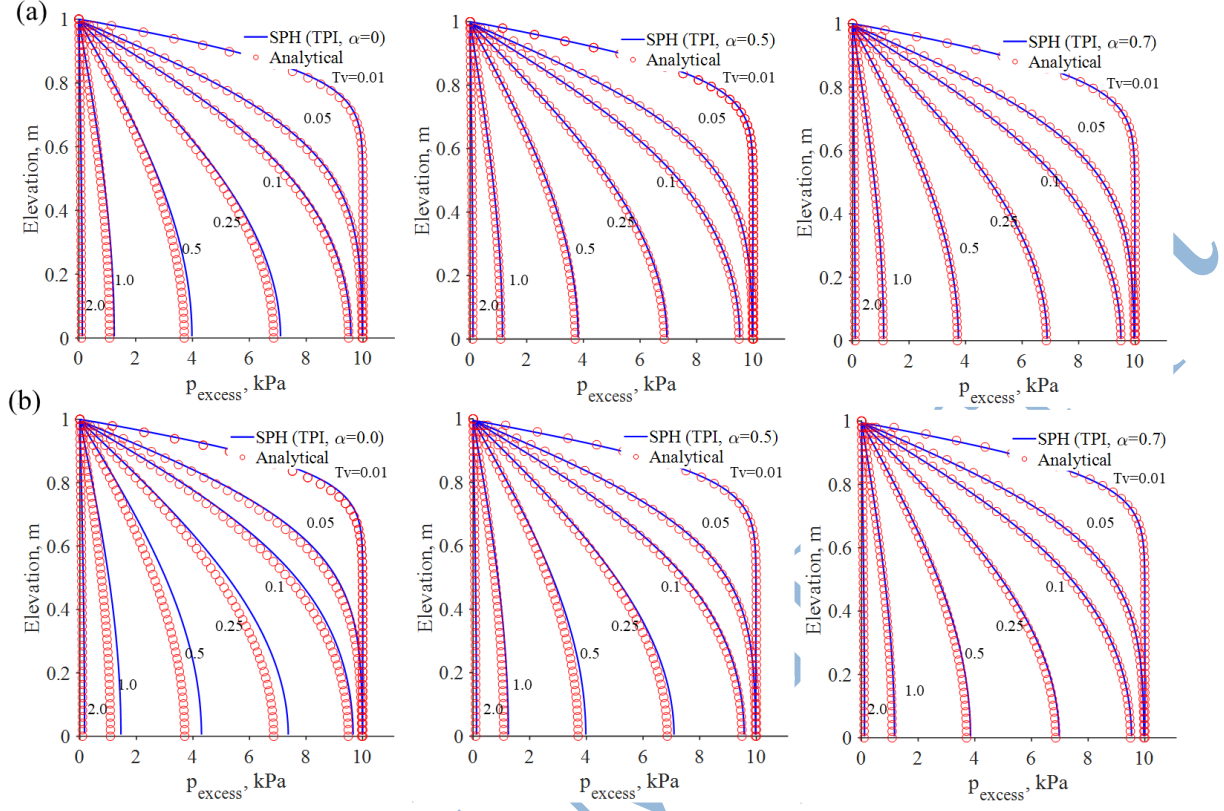


Fig. 4 The SPH simulation with the proposed time integration scheme of the evolution of the excess pore-water pressure for different time intervals: (a) $\Delta t = 5 \times 10^{-6} s$; (b) $\Delta t = 1 \times 10^{-5} s$

An extreme case is also considered by increasing the time step size by $R = 35$ times to $\Delta t = 1 \times 10^{-5} s$ (i.e., compared to the fully explicit solution), which is close to the capped timestep size defined by the CFL condition (41) for the solid phase. The results of this simulation with different values of α are reported in Figure 4(b). Higher errors can be noticed in the result predicted by Eq. (37), which is expected since the assumption of $p_{l_j}^{t+1} \approx p_{l_j}^t$ is less acceptable in such large timestep size. On the other hand, the proposed formulation (38) with $\alpha = 0.5$ produces a comparable result with some minor errors, and these errors can be removed by further increasing the value of α to 0.7 . The result indicates that the proposed TPI can handle a large timestep size that is close to the capped timestep size defined by the CFL condition (41) for the solid phase in the fully coupled flow-deformation analysis. As we continue to increase the timestep size, the accuracy of the TPI scheme will further reduce, and the numerical solution becomes unstable for $\alpha = 0$ (i.e., $R > 250$) and for a larger α value (e.g., $R = 98$ and $\alpha > 0.75$). However, because the maximum timestep size in the current SPH application is

capped by the timestep size defined by the CFL condition (41) for the solid phase, the adopted timestep must not violate this condition. The above results suggest that the proposed TPI integration technique offers an excellent way to achieve stable solutions and reduce the computational cost compared to the fully explicit time integration method (i.e., at least an order of magnitude faster for high permeability applications and even much higher for applications with larger permeabilities). The computational efficiency of the proposed TPI algorithm could be much higher than those reported in this paper if one adopts a higher CFL coefficient (C_{CFL}), which is 0.1 in our work compared to 0.5 adopted in other works [38]. Given that the current paper adopts the small-strain formulation, a small CFL coefficient is recommended to ensure the objectivity of stress increments when dealing with large deformation problems. With such a small C_{CFL} , the proposed TPI scheme can be confidently used with $\alpha = 0.5 - 0.7$ as demonstrated above, although $\alpha = 0.5$ is recommended for applications involving fast loading rate. In the rest of applications presented in this paper, the proposed TPI scheme with $\alpha = 0.5$ is adopted to demonstrate the effectiveness and stability of the proposed TPI scheme.

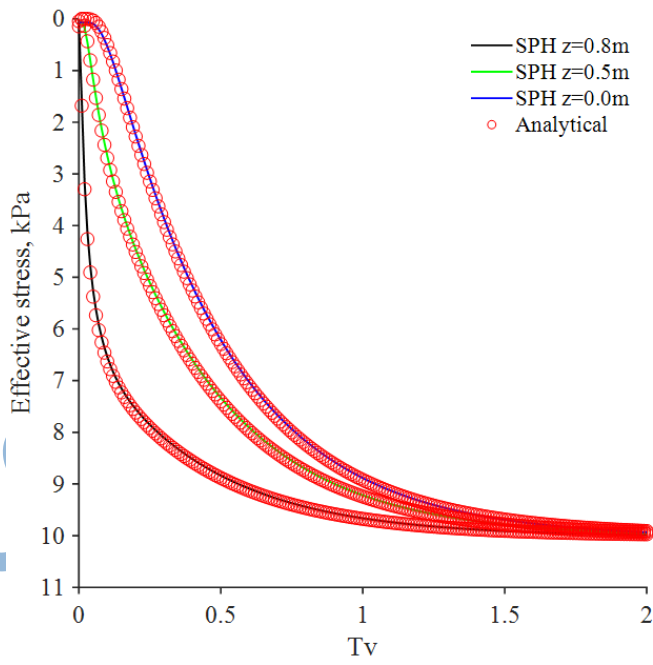


Fig. 5 The evolution of the effective stress in the soil column

4.2 Verifications through 1D harmonic consolidation problem

In this case, a more challenging coupled flow-deformation problem, namely 1D harmonic consolidation, is considered. The challenge of this example lies in how the proposed model predicts the excess pore-water pressure in the soil against complex dynamic loading and

drained conditions. This interesting test was first studied in [64] and later in [46,65], to name a few, where the analytical solution based on the $(\mathbf{u} - \mathbf{w} - p_l)$ formulation are available. Numerical studies have also been conducted based on either $(\mathbf{u} - \mathbf{w} - p_l)$ formulation [66] and $(\mathbf{u} - \mathbf{w})$ version [48,67], and these existing results will be used as reference solutions for comparisons.

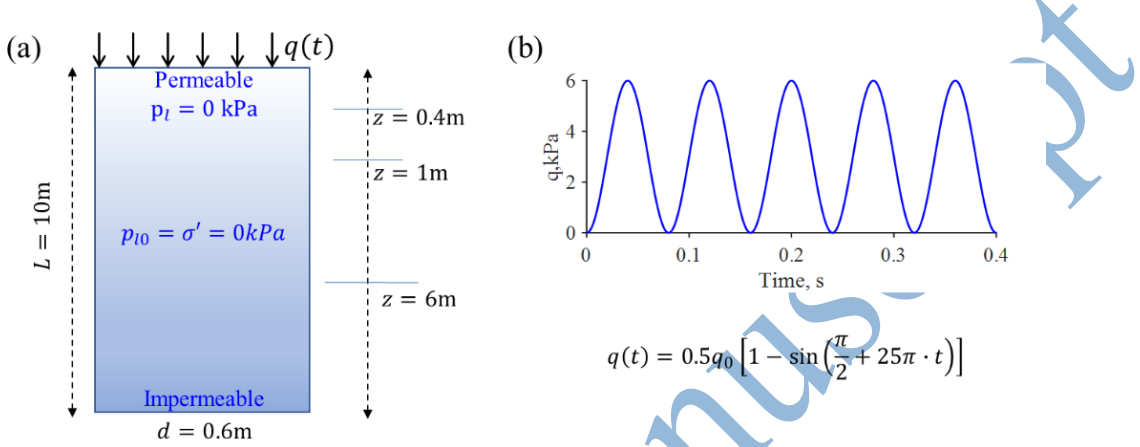


Fig. 6 SPH model of the 1D harmonic consolidation problem. (a) The geometry condition; (b) the diagram of the harmonic loading function

The geometry of the problem and the period loading function is given in Figure 6(a). The soil column is initialised with zero effective stress and zero pore-water pressure. The zero value of pore-water pressure on the top surface is kept unchanged during the computation to simulate the fully drained condition. The soil sample is modelled using 2000 particles with an initial space distance of 0.04m. For a comparison purpose, all the material properties are set as the same as the early study in [65] as follows: Young's modulus $E = 30 \text{ MPa}$, Poisson's ratio $\nu = 0.2$, porosity $n = 0.33$, fluid bulk modulus $K_l = 1 \text{ GPa}$, and density $\rho_s = 2000 \text{ kg/m}^3$. The water density $\rho_l = 1000 \text{ kg/m}^3$, and the saturated permeability $k_{sat} = 1 \times 10^{-2} \text{ m/s}$, which is kept constant for the entire computation. The soil is treated as an elastic material, and gravity is neglected. The global damping coefficient $\eta_d = 0.02$ is considered. The simulation is conducted with a time step size of $\Delta t = 4 \times 10^{-7} \text{ s}$ and the stabilisation coefficient $\alpha = 0.5$. It is worth noting that the timestep adopted in this case is about $R \approx 5$ times larger than that given by the fully explicit integration algorithm defined in Eq. (42) for the flow phase. It is also noted that no pore-pressure regularisation technique is applied in this case.

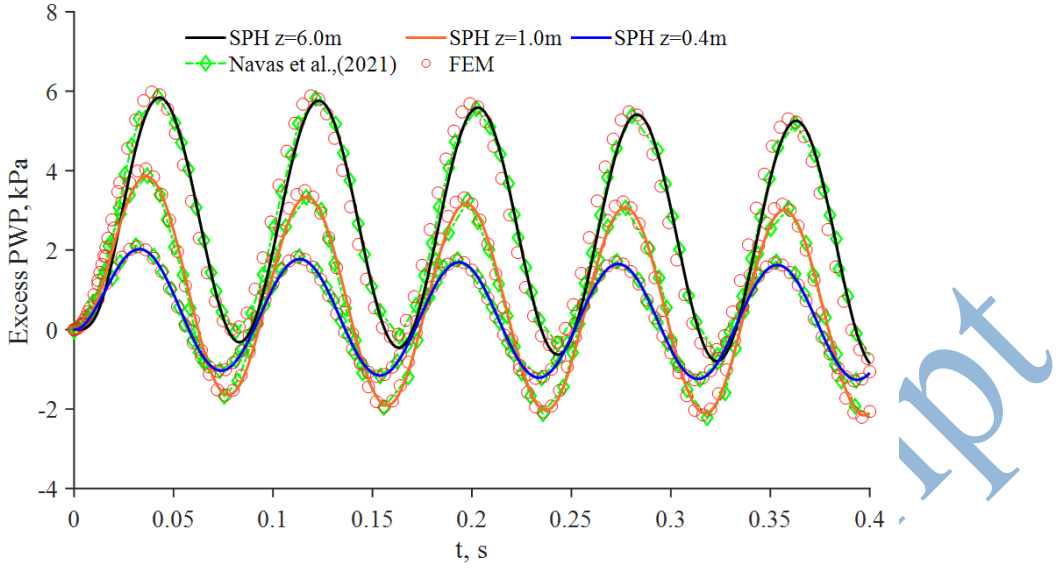


Fig. 7 *The evolution of excess pore water pressure in the harmonic consolidation test*

Figure 7 shows the predicted evolution of excess pore-water pressure at various depths in the soil column. It is seen that the result obtained using the proposed SPH method agrees reasonably well with the FEM and other reference solutions [68]. For example, a sinusoidal shape curve of the excess pore-water pressure corresponding to the harmonic loading is observed, in which different peak values associated with the various depth are also captured. The peak excess pore-water pressure at each location gradually decreased due to the dissipation on the upper surface. It is also interesting to find some negative excess pore-water pressure in the vicinity of the upper surface (i.e., mostly with $z = 0.4\text{m}$ and 1.0m). This negative excess pressure is computed because the gravity acceleration and the initial condition from the geostatic loading were neglected. At the same time, it also can be attributed to the recovery of the elastic deformation near the surface of the soil column, i.e., the relief of compression can cause the expansion of the pore, which subsequently leads to the absorption of the water content, causing negative excess-pore water pressure [66]. The marginal difference among results presented in Figure 7 is mainly due to the difference in the time integration scheme and formulation used to achieve numerical solutions of the coupled problems.

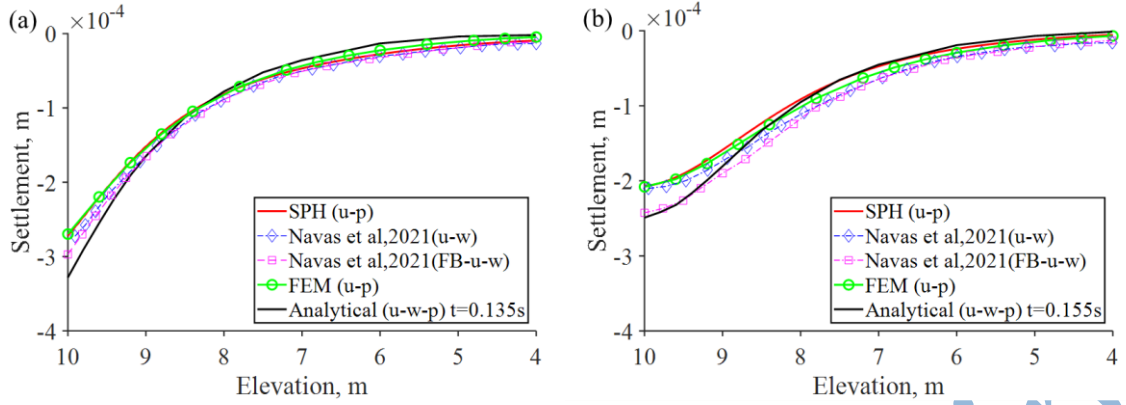


Fig. 8 The settlement profile along the soil column at different time intervals: (a) $t = 0.135s$; (b) $t = 0.155s$.

Besides the prediction of excess pore-water pressure, the settlement along the soil column is also well captured by the model, as shown in Figure 8. In two different instances, i.e., $t = 0.135s$ and $0.155s$, the predicted deformation by the proposed coupled SPH framework agrees well with the reference solutions [65,67]. For example, the present framework yields close results to the ones by FEM [68] and Navas et al. [67], which are based on the $(\mathbf{u} - p_l)$ and $(\mathbf{u} - \mathbf{w})$ formulations, respectively. This is because the current application is classified as low-frequency dynamic consolidation problem [46], where the dynamic term (i.e., the relative acceleration term in Eq. (6)) can be neglected; therefore, both $(\mathbf{u} - p_l)$ and $(\mathbf{u} - \mathbf{w})$ formulations share similar results [67]. Some noticeable differences lie in the maximum settlement, which may be attributed to the volumetric locking effect associated with the incompressible fluid and grain, different coupling formulations or large strain deformation formulation [67]. For example, the analytical solution in Figure 8 given by De Boer and his co-workers [65] was obtained by using the $(\mathbf{u} - \mathbf{w} - p_l)$ formulation, whereas the present solution is obtained by using the $(\mathbf{u} - p_l)$ formulation, which is also similar to the $(\mathbf{u} - \mathbf{w})$ formulation. To mitigate this error in the maximum surface displacement, the $(\mathbf{u} - \mathbf{w} - p_l)$ formulation or other stabilisation methodologies, i.e., large strain concept to address the volumetric locking (i.e., $FBar - \mathbf{u} - \mathbf{w}$ formulation in the figure) [67], could be considered, which is out of the scope of this study. Nevertheless, our proposed method effectively captures the evolution of excess pore-water pressure and deformation in this challenging harmonic consolidation problem, which is the first ever achieved solutions by SPH to our best knowledge.

4.3 2D flexible strip loading

A flexible strip footing problem on the fully saturated soil layer is considered in this section. The geometry of this problem is given in Figure 9. The soil layer is $8a$ in-depth and $16a$ in width and is large enough to eliminate the boundary effect [69]. The width of the strip footing is a , and $a = 1.25m$ is used in this simulation. The left and the right boundaries are free-slip and can be modelled by ghost particles [11]. The bottom boundary is fixed in horizontal and vertical directions, which can also be modelled by the solid boundary particles [11]. Besides, all the boundaries, including the bottom of the strip footing, are impervious within the ramp-load stage (i.e., when $t \leq t_L$ in Figure 9(b)). After completing the ramp-loading process, a fully permeable condition is enforced to the upper open surface of the soil layer by imposing a zero pore-water pressure condition to trigger the pore-water pressure dissipation process, whereas other boundaries are kept as impermeable. The following material properties are used: Young's modulus $E = 20 MPa$, Poisson's ratio $\nu = 0.33$, porosity $n = 0.40$, fluid bulk modulus $K_l = 1 GPa$, and density $\rho_s = 2650 kg/m^3$. The water density $\rho_l = 1000 kg/m^3$ and the saturated permeability $k_{sat} = 1 \times 10^{-3} m/s$. The global damping coefficient η_d is 0.04. A total of 20,000 particles with an initial particle spacing of $dx = 0.1m$ are used, and due to the high permeability, the time step size is dominated by the flow phase. This simulation is conducted using the proposed TPI algorithm ($\alpha = 0.5$) with a constant timestep size $\Delta t = 1 \times 10^{-4}s$, which is nearly $R = 15$ times larger than the explicit CFL time step size (condition (42)) for the flow phase. Additionally, no pore-pressure regularisation technique is required and the gravity acceleration is ignored in this case.

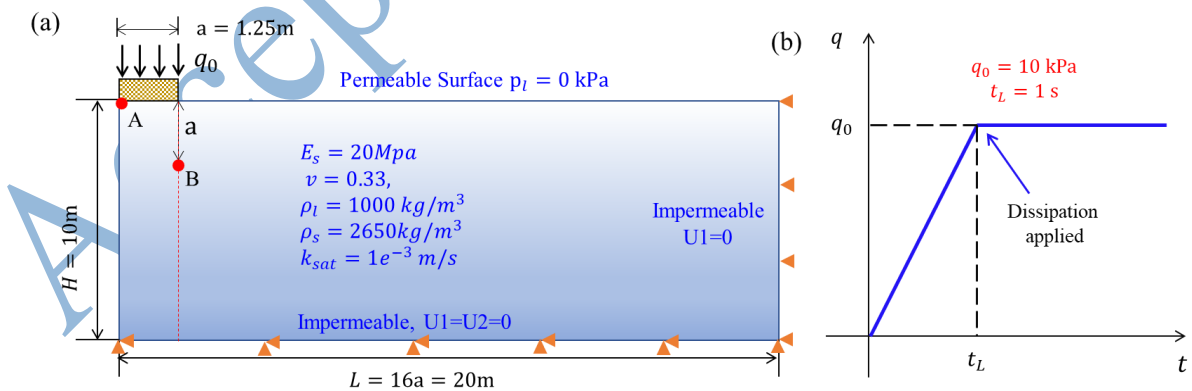


Fig. 9 The diagram of the 2D flexible strip footing problem. (a) Geometry and boundary conditions
(b) the ramp loading process.

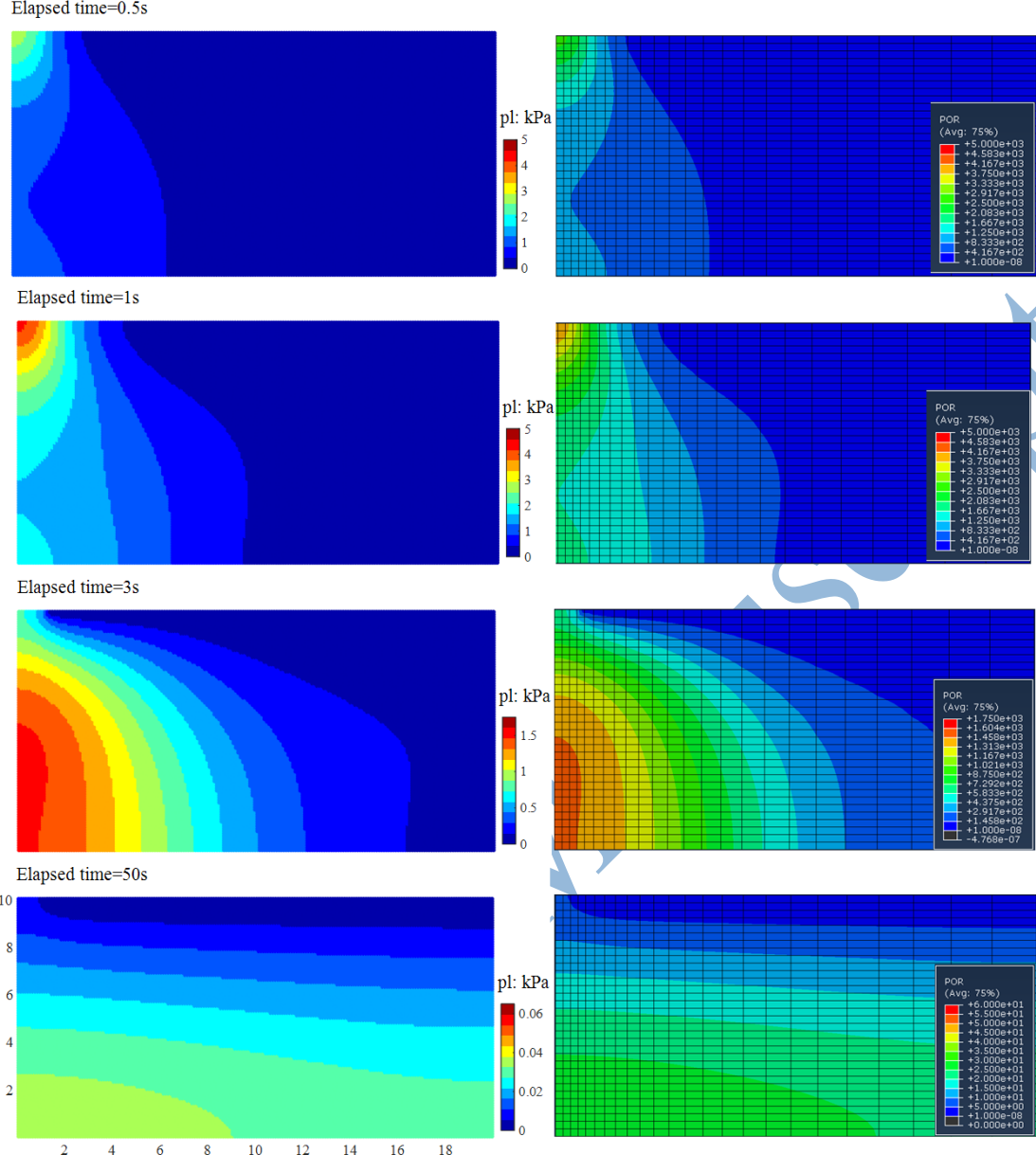


Fig. 10 The evolution of excess pore water pressure in the 2D flexible strip footing.

Figure 10 shows the contour plot of the excess pore-water pressure development and dissipation in the soil layer predicted by SPH and FEM. The FEM solutions were obtained using the commercial ABAQUS software package. The same boundary conditions and soil parameters given in Figure 9 were adopted in the FEM simulation, with numerical solutions obtained using the standard/explicit solver provided by ABAQUS. It can be observed that the excess pore-water pressure builds up under the footing within the loading compression stage and dissipates after the drained condition is applied. SPH obtains a very stable and smooth pore pressure distribution thanks to the adopted stabilisation technique (i.e., the global damping force), which dissipates the unwanted dynamic energy of solid particles, thus enabling the

current framework to be free from the pressure fluctuation reported in the earliest coupled flow-deformation SPH framework [34]. The evolution of excess pore water pressure at Points A and B are given in Figure 11, where the results match well with the reference FEM solutions, indicating that our model could capture well both the excess pore water pressure built-up and dissipation. For example, within the ramp-load stage ($t \leq t_L$), excess pore-water pressure is generated due to the volumetric compaction and reaches its peak value when $t = t_L$. The peak value of excess pore water pressure at Point B is less than that at Point A because Point B is located deeper and further from the strip centre. After completing the ramp load, the excess pore water pressure starts to dissipate and entirely dissipates at $t = 100$ s, during which the predicted excess pore water pressure matches well with the reference solutions (see Figure 11). The settlement at Points A and B are shown in Figure 12(a), where the predicted deformation by the proposed SPH method again agrees well with the reference FEM solution. More convincingly, the calculated horizontal displacement along the section under the right edge of footing (Marked by the red ‘--’ line in Figure 8(a)) is also well matched with the FEM solution, as shown in Figure 12(b).

These excellent agreements against FEM solutions suggest that the proposed SPH framework utilising the TPI algorithm could capture well the coupling behaviour of saturated soils and is ready for more complex coupled hydromechanical analysis involved with large deformation, which will be presented in the next section.

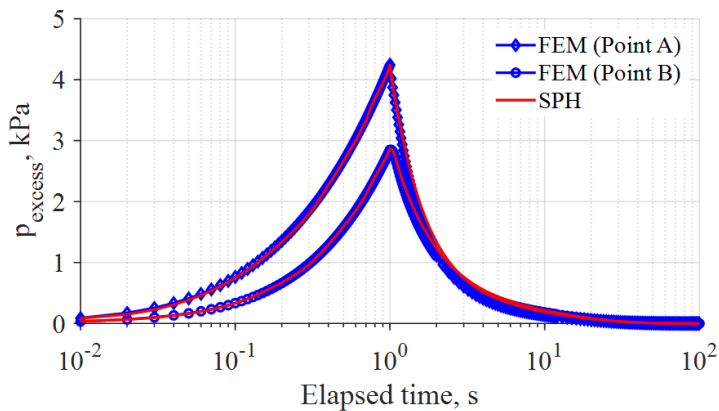


Fig. 11 The evolution of excess pore-water pressure in the 2D flexible strip footing.

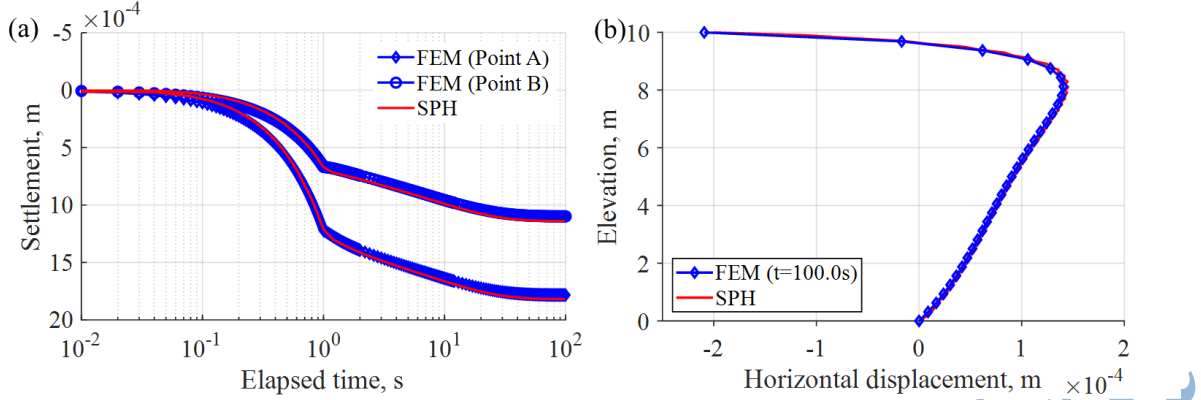


Fig. 12 SPH prediction on the deformation in the 2D strip footing test: (a) settlement at Points A and B; (b) horizontal displacement versus depth along the vertical section passing Point B under the right edge of the footing

4.4 Granular collapse of saturated soils

In this example, the simulation of granular collapse on saturated soil columns is considered to demonstrate the capability of the proposed method for fully coupled analysis involving large deformation in geotechnical applications. The same geometry as the earliest work on SPH modelling of granular collapse by Bui et al. [11] is considered and shown in Figure 13(a). However, different from the work by Bui et al. [11], in this study, the soil is considered initially fully saturated with a pre-described water table on the upper surface (see Figure 13(b)). The importance of this example lies in how the proposed model predicts the excess pore water pressure that varies against the dilatancy angle and the deformation pattern of the shear band. To replicate these phenomena, three dilatancy angles of $\psi^{peak} = 0^\circ$, 2.5° and -5° , corresponding to non-dilative soils, purely dilative soils, and purely contractive soils, are considered.

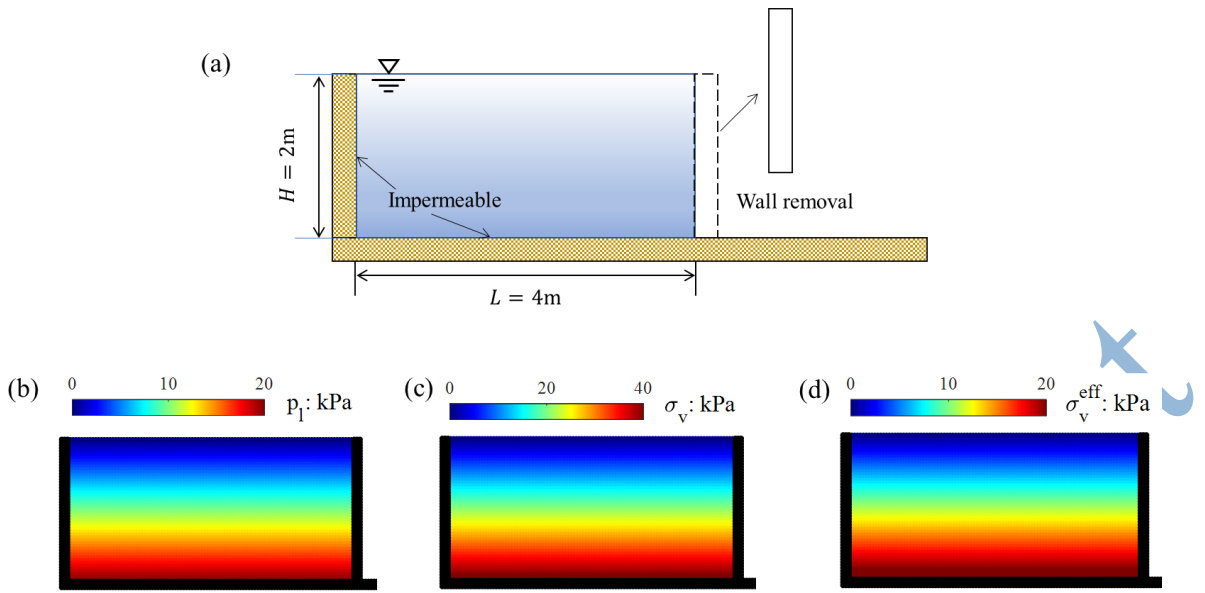


Fig. 13 Schematic of the geometry for the granular collapse of fully saturated soil

Table 1. Material properties of the granular column collapse of saturated soil

Material properties	Soil types		
Young's modulus (E_s), MPa	20	20	20
Solid density, (ρ_s), kg/m ³	2650	2650	2650
Poison's ratio, ν	0.33	0.33	0.33
Porosity, (n)	0.35	0.35	0.35
Water bulk modulus, (K_l), GPa	1	1	1
Water density, (ρ_l), kg/m ³	1000	1000	1000
Saturated permeability, (k_{sat}), m/s	0.0002	0.0002	0.0002
Kozeny-Carman coefficient, (C_k)	2	2	2
Peak or residual friction angle, (ϕ_p, ϕ_r), °	25	25	25
Peak cohesion, (c_p), kPa	5	5	7.5
Residual cohesion, (c_r), kPa	1	1	1
Softening constant, (η)	5	5	5
Dilation angle, (ψ_0), °	0	2.5	-5
Dilation softening constant, (s_f)	N/A	0.2	0.2
Stabilization coefficient, (α)	0.5	0.5	0.5

The simulations are performed using 5000 particles with an initial spacing distance of 0.04m. Three walls are modelled by either the free-slip boundary (the left and the right walls) or the solid boundary (the bottom) [11], and all the walls are impermeable, of which the condition can be modelled following the work recently proposed by the authors [36]. As for the hydraulic condition on the free surface, the proposed free-seepage surface boundary treatment in [36] and the ponding condition of $p_l \leq 0$ are also adopted in this study. The soil behaviour is modelled by the elasto-plastic Drucker-Prager (DP) softening model for the demonstration purpose, though more advanced constitutive models can be readily incorporated in SPH [3], and the material properties are given in Table 1. Due to the large permeability of the soil, the proposed semi-implicit integration scheme is adopted in this example. After the initial in-situ total and effective stress conditions are obtained by applying gravitational load to the soil column (see Figures 13(c) and 13(d)), the right wall is then suddenly removed to trigger the collapse. The simulation is conducted with a time increment as 2×10^{-5} s, which is nearly 5 times larger than the fully explicit CFL time step given in condition (42).

The first simulation is carried out with a zero dilatancy angle. The shear band development and the evolution of excess pore water pressure induced by plastic volumetric deformation are shown in Figure 14. After removing the right wall, the reduction of lateral pressure resulted in a circular shape shear band that developed and propagated backward the back scarp, forming multiple failure surfaces. A retrogressive failure was then observed, with the soil column undergoing flow-sliding behaviour. No excess pore water pressure is generated in the shear band zone, which can be attributed to the fact that a zero dilatancy angle was adopted in this simulation. The proposed model accurately predicted this response of excess pore-water pressure for no volumetric plastic strain developed in the model. Despite this fact, the failure pattern of the saturated soil column in this fully coupled analysis is different from that in the dry soil by Bui et al. [11], which can be attributed to pore-water pressure in the current simulation.

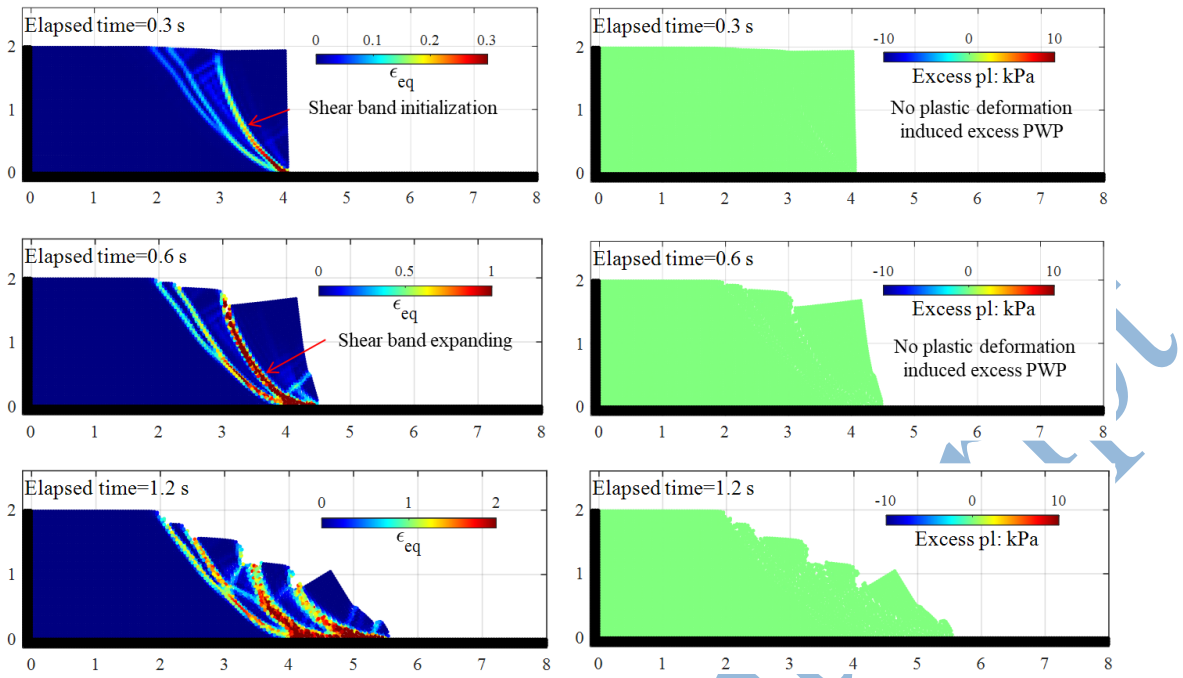


Fig. 14 Granular collapse of fully saturated soil with dilatancy angle $\psi^{peak} = 0^\circ$

The second simulation is performed with a positive dilatancy angle of 2.5° , i.e., dilatative soils. Figure 15 shows the equivalent accumulated plastic strain profiles and the evolution of excess pore-water pressure caused by plastic volumetric dilation of the simulated soil during the post-failure process. The proposed method captures the intended negative excess pore-water pressure developing inside the shear band caused by volumetric plastic dilation. For example, the negative excess pore-water pressure is first observed along the shear band and continually increases as the shear band further develops (i.e., from 0.3s to 0.6s). However, at the final stage, when the collapse stopped at $t = 1.2\text{s}$, the excess pore-water pressure inside the shear band undergoes some dissipation, which can be attributed to the increase of porosity caused by large shearing deformation and thus increasing the permeability, facilitating the excess pore-water pressure dissipation process. It is noted that even though the same parameters with the first case (except the dilatancy angle) are used, a different failure pattern is observed in this case. This can be attributed to the development of negative excess pore-water pressure, causing an increase in the mean effective stress, and thus affecting the final deformation pattern. As the positive dilatancy angle is further increased, for example, to 5° , no collapse was observed in the simulation, which can be again attributed to the development of negative excess pore-water pressure.

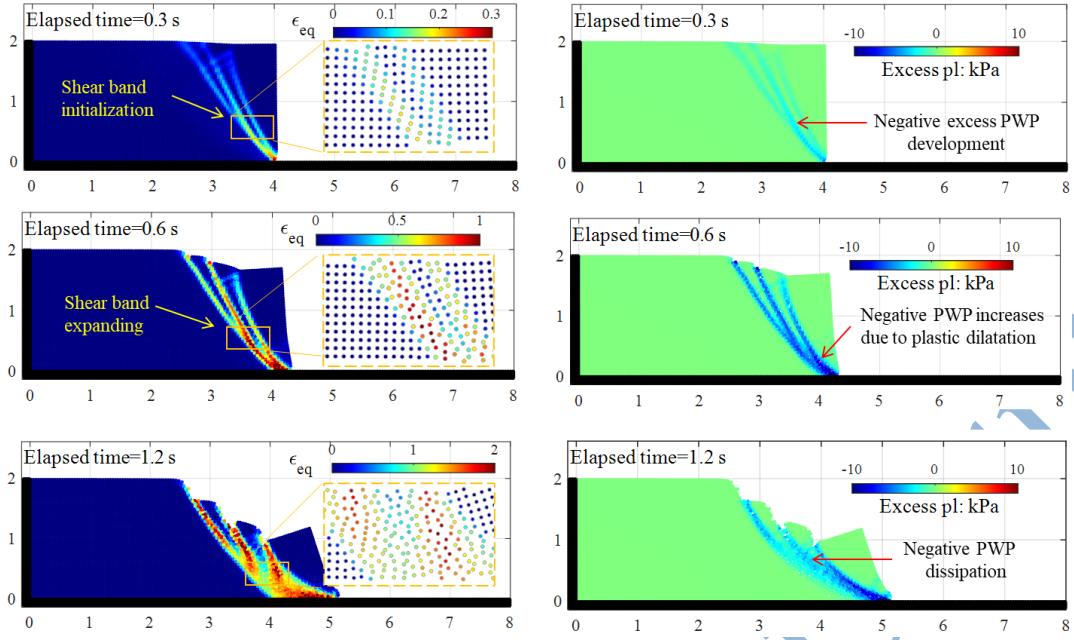


Fig. 15 Granular collapse of fully saturated soil with dilatancy angle $\psi^{peak} = 2.5^\circ$

The effectiveness of the proposed negative pore-water pressure stabilised technique is demonstrated in Figure 16, in which a comparison is made between the stabilised and non-stabilised cases. After releasing the gate, water flows out of the soil column due to the relatively high permeability adopted in this example. This forms a well-defined curvature phreatic line, above which the pore-water pressure is zero because unsaturated seepage was not considered in the current water-saturated SPH formulation. The soil above the phreatic line subsequently underwent volumetric dilation, and thus negative pore-water pressure (i.e., equal to excess pore-water pressure in this case) was predicted. The development of negative pore-water pressure is over-predicted in the SPH model without adopting the stabilised procedure, resulting in non-physical behaviours of the soil, as shown in Figure 16(b). On the contrary, the proposed stabilisation technique helps maintain the change rate of the negative excess pore-water pressure and thus stabilises the SPH solution, where the collapse of the soil column is still processed.

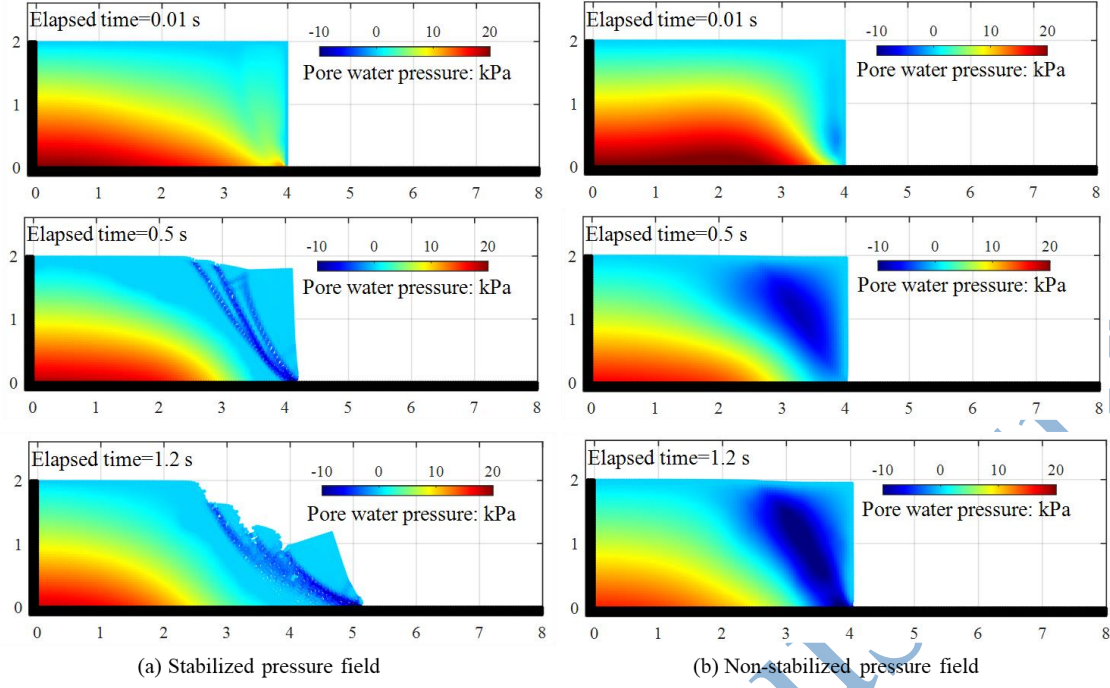


Fig. 16 Pore fluid pressure field in the dilative soil

In the last example, a negative dilatancy angle -5° standing for the contractive soils is considered, and the simulated results are presented in Figure 17. In contrast to the dilative soil, the positive excess pore-water pressure caused by volumetric plastic contraction is now observed within the shear band, as shown at the beginning at $t = 0.2s$. The development of positive excess pore-water pressure reduces the effective stress to nearly zero (i.e., liquefaction), which subsequently triggers a rapid flow of the sliding band at $t = 0.5s$. As the soil undergoes large shearing deformation associated with high volumetric compaction, more excess pore water pressure is generated, weakening the soil, and eventually leading to complete liquefaction (i.e., the shear strength could drop to zero). As a result, a very rapid liquid-like sliding failure behaviour characterised by a longer run-out distance is observed, as shown in Figure 17 at $t = 1.6s$. As the liquefied sliding mass flows away, the back scarp soils lost their lateral support and continued to collapse, undergoing liquefaction, and replicating the fluid-like behaviour until the complete failure stopped at around $t = 3.0s$.

Overall, the above simulations demonstrated the capability of the proposed computational approach in handling the complicated coupling mechanisms associated with large soil deformation and failure relevant to geotechnical engineering applications.

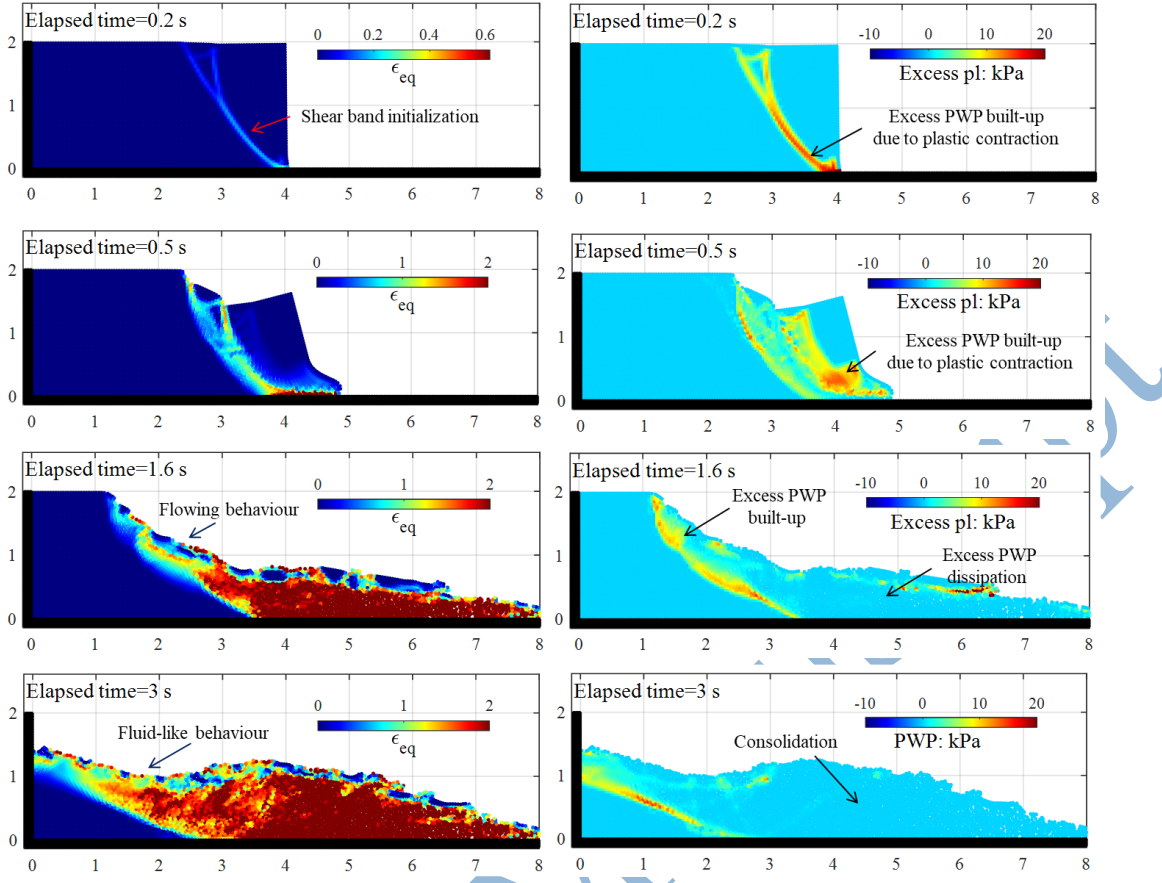


Fig. 17 Granular collapse of fully saturated soil with dilatancy angle $\psi^p = -5^\circ$

4.5 Coupled modelling of retrogressive failure of sensitive clay

In this section, the capability of the computational framework in predicting coupled behaviour of geomaterials undergoing large deformation and post-failure is further demonstrated through the modelling of retrogressive failure of slope in sensitive clays. This large-scale progressive failure of quick clays frequently occurs worldwide, especially in eastern Canada and Scandinavia [70], where sensitive clays are commonly found. The collapse of this clay slope is often characterised by its rapid motion, long travel distance, and the strong strain-softening behaviour of the soil [70]. Field observations, conceptional modelling, and analysis have been frequently reported in the past several decades [70–73]. Among these studies, retrogressive landslides are often classified into three main types: flow, translational and spreading failures [70,71]. On the other hand, modelling of retrogressive failure has also gained much interest, and several advanced numerical methods, i.e., SPH, Material Point Method (MPM), and Smoothed Particle Finite Element Method (PFEM), to name a few, have been applied to analyse these challenging problems with certain successes recently [3,74–79]. In those attempts, the initially stiff state of the clay was always assumed to turn into the semi-liquid or liquid state

quickly, and this “assumed” transition state was achieved by imposing the undrained condition using a zero-friction angle and a large Poisson’s ratio (i.e., $\nu = 0.495$). Thereafter, a strain-softening model was adopted to describe the rapid motion and long run-out distance [3,74–79]. The key limitation of these works is that the development of excess pore-water pressure and its influence on retrogressive failure was not considered, which might not be reasonable for sensitive clays [45]. More recently, Jin & Yin (2022) [45] investigated the effect of excess pore water pressure on the retrogressive failure mechanism. However, the excess pore water pressure in their approach was computed from the Effective Stress Analysis Method instead of by solving the fully coupled pore-water pressure equation; thus, improvement is still needed to better understand the pore-water pressure generation and dissipation processes during the post-failure process. This study applies the proposed coupled flow-deformation SPH framework to investigate this problem further. To our best knowledge, this will be the first attempt to solve this retrogressive failure of clays using the fully coupled hydromechanical approach, in which the evolution of excess pore-water pressure and its dissipation is fully described and kept track during the entire failure process.

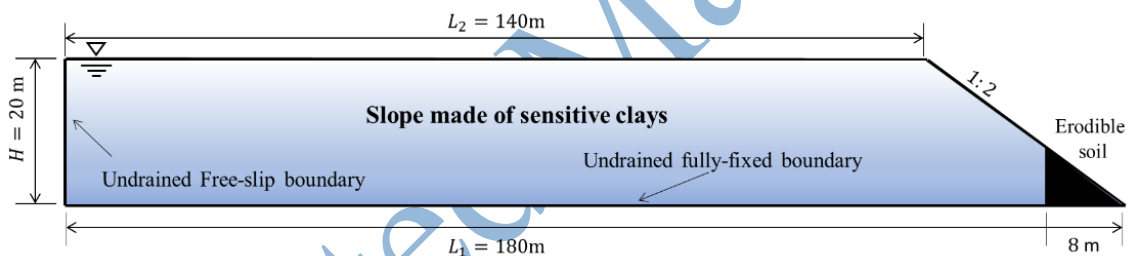


Fig. 18 *Geometry and boundary condition of a slope made of sensitive clays*

The geometry for the representative cross-section of a slope made of sensitive clays is outlined in Figure 18. The slope is 20 meters in height and 180 meters in length, with the slope angle being 27° . A pre-described water table is introduced to the ground surface to replicate the fully saturated condition of the clay, as shown in Figure 18. The material properties of the saturated sensitive clay are given as follows: Young’s modulus $E = 12.5$ MPa; solid-phase density $\rho_s = 2650 \text{ kg/m}^3$; Poisson’s ratio $\nu = 0.33$; the initial peak shear strength $\phi'_p = 10^\circ$ and $c_{peak} = 55 \text{ kPa}$; the residual shear strength $\phi_{res} = 5^\circ$ and $c_{res} = 0.7 \text{ kPa}$, with the softening coefficient η being 5; water density $\rho_l = 1000 \text{ kg/m}^3$; porosity $n = 0.4$; fluid bulk modulus $K_l=1\times 10^8 \text{ Pa}$; permeability $k_{sat}=5\times 10^{-8} \text{ m/s}$, with the coefficient $C_k = 2$. As reported in the field observations [70], the angle of horsts formed in the field ranges from $\theta = 50^\circ$ to 68° ,

indicating that the effective friction angle of sensitive clays ranges from $\phi'_p = 10^\circ$ to 46° (i.e., based on the Mohr-Coulomb failure theory $\theta = 45^\circ + \phi'_p/2$). Therefore, in this paper, the effective friction angle of $\phi'_p = 10^\circ$ is selected for the demonstration purpose. On the other hand, the permeability of clay soil is usually very low ($\sim 10^{-8} \text{ m/s}$), thus the fully explicit time integration scheme is suitable and chosen in this case. It is also noted that the shear strength of the sensitive clay might increase among the depth [80]. In this study, it is simplified assumed to be uniformly distributed across the entire slope. More importantly, different from all previous studies which imposed the undrained condition by having a zero friction and dilatancy angles [3,74–79], the drained analysis with extremely low permeability is considered herein, and a negative dilatancy angle $\psi = -5^\circ$ with softening coefficient s_d being 0.50 is further adopted, thus the influence of excess pore-water pressure on the failure mechanism can be assessed.

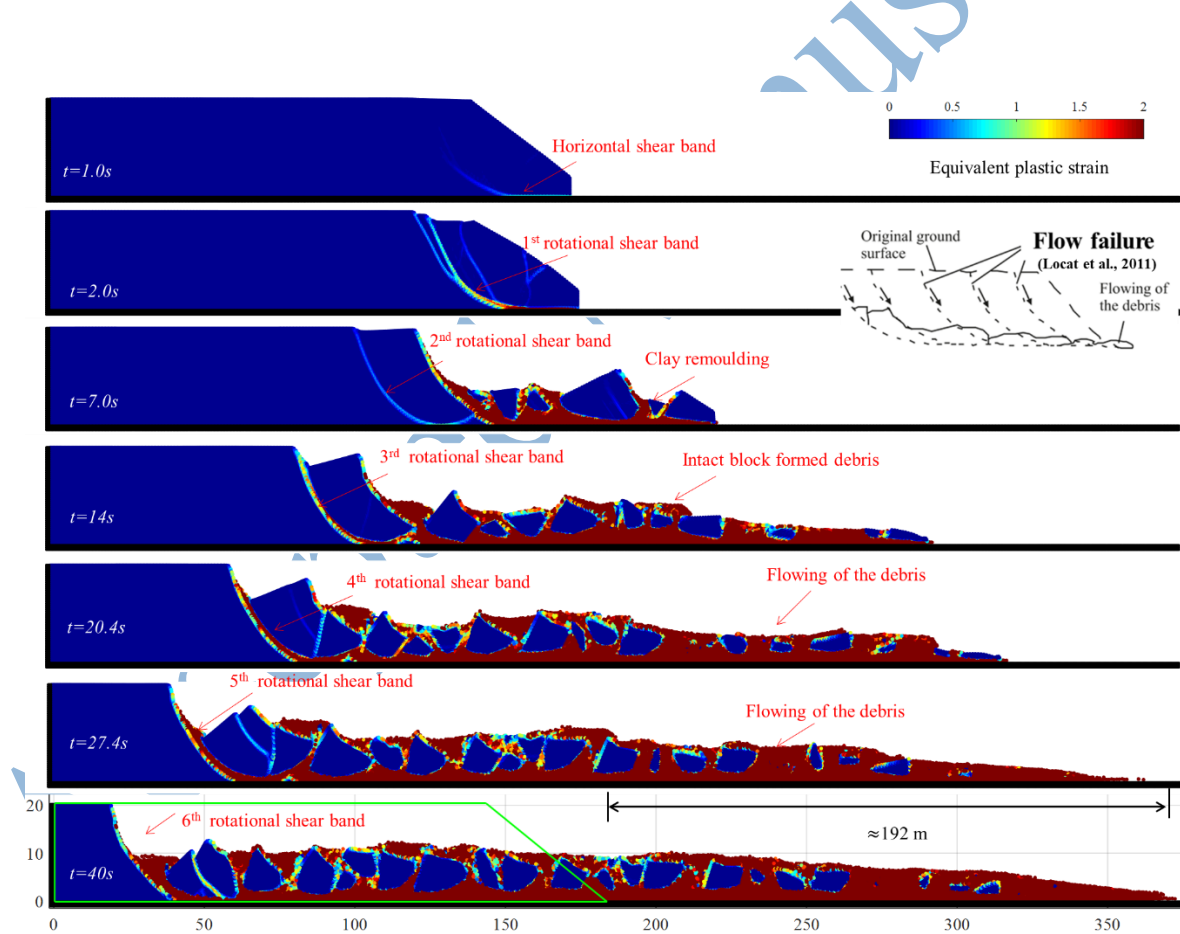


Fig. 19 Stabilised SPH prediction of the retrogressive failure of sensitive clay slope with $K_0 = 0.5$.

The studied slope is modelled using 20349 SPH particles, with an initial particle spacing of 0.4m. The free-slip vertical and fixed-bottom boundaries are modelled respectively by the

ghost and virtual particles [11], where the undrained boundary condition is also enforced following the original approach reported in [36]. Due to the relatively low permeability in the clay, the time step size will be capped by the solid phase given in condition (38), where the time step size is 4×10^{-4} s. The simulation is performed in two steps. First, a global water table is assigned to the slope to obtain the steady-state hydraulic condition, followed by gravitational loading to obtain the initial in-situ stress conditions. It is reported that the lateral pressure coefficient at rest (K_0) highly influences the successive retrogressive failure of the sensitive clay, but investigations on its influence in sensitive clay is still limited [79]. Therefore, the simulation is performed with different K_0 values to investigate its influence on the types of retrogressive failure. Based on some field tests, K_0 of sensitive clay is ranged from around 0.6 to 3.5 [81]. In this study, $K_0 = 0.5$ and 1.5 are considered. After the initial stress condition is achieved (which will be given in the result analysis below), a portion of the slope toe is removed to mimic the erosion induced retrogressive failure, which is commonly adopted in the literature [45,74,79].

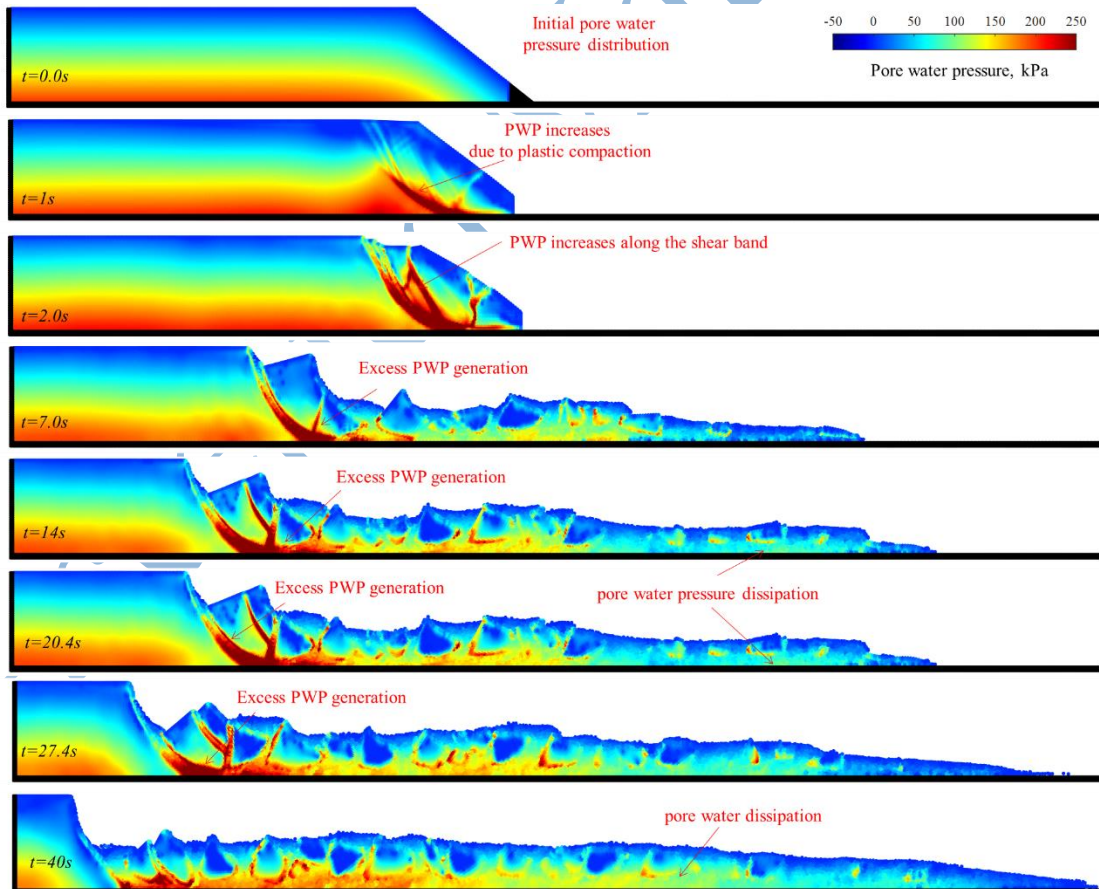


Fig. 20 Stabilised SPH prediction of the pore water pressure induced by contraction in the retrogressive failure of sensitive clay slope with $K_0 = 0.5$.

Figure 19 shows the progressive failure of the slope predicted by the proposed SPH model with the lateral earth pressure coefficient of $K_0 = 0.5$. The corresponding pore-water pressure and mean effective stress profiles are given in Figures 20 and 21, respectively. The proposed framework successfully captures a flow-sliding type retrogressive failure without requiring the undrained assumption commonly adopted in the literature, with a stable description of the pore-water pressure and effective stress in this case. For example, after removing the erodible soil block from the slope toe, a horizontal shear band develops inward the slope at the bottom, propagating upward and forming the 1st rotational sliding surface at $t = 2.0\text{ s}$. The moving soil mass is also strongly remoulded and rapidly flowing out of the crater. This flowing debris removed the lateral support to the remaining slope, leaving an unstable scarp, where subsequently the 2nd rotational slide occurs in a similar way at $t = 7.0\text{ s}$. At the same time, similar behaviour of pore water pressure and effective stress is again observed in the sensitive clay, as shown in Figures 20 and 21, respectively. The same failure process is repeated for subsequent sliding blocks until the volume of debris materials building up in front of the crater is large enough to provide sufficient lateral support to the remaining slope, thus forming a final stable back scarp at $t = 40\text{ s}$. A total of 6 rotational slides are observed, with the size of each sliding mass being similar to each other, which is mainly attributed to the assumed homogenous material properties. The final run-out distance reaches 192 m. It is worth noting that the above results can only qualitatively predict the shear band formation and evolution process. To adequately capture this process, one needs to consider the bifurcation condition to initiate the localised failure and suitable constitutive models to account for the length scale of the problems (i.e., the shear band orientation and thickness). Such considerations are beyond the scope of the current paper.

Nevertheless, it is interesting to notice the dissipation of excess pore-water pressure within the flowing debris (see Figure 20), which can be attributed to the porosity change in the soil after undergoing large deformation, thus causing permeability to increase, facilitating the dissipation process of excess pore water pressure. This dissipation process can represent the consolidation stage associated with an increase in effective stress (see Figure 21), which gradually stops the flowing behaviour of the clay soil. It is worth noting that this dissipation/consolidation process within the clay slope failure could only be achieved by the fully coupled flow-deformation framework, which outperforms the undrained approaches [70–73]. Overall, the predicted failure mode is well consistent with the flowing failure from the on-site observation [70], as shown in Figure 19. On the other hand, the retrogressive failure of sensitive clay slopes ($K_0 =$

0.5) predicted using the non-stabilised SPH model is shown in Figure 22. This result demonstrates the effectiveness of the proposed stabilisation technique to achieve a smooth pore-water pressure field for the proposed water-saturated SPH formulation achieved in Figure 20. For non-stabilised solutions, the instability in the development of pore-water pressure (i.e., pressure noise) is noticeable across the computational domain as soon as the 1st slide failure occurs, with more severity concentrated on the areas where the soil undergoes large deformation. The instability in the pore water pressure field becomes more apparent, especially in the area close to the left boundary, as the retrogressive failure processing (i.e., $t = 14.0$ s and 27.4 s).

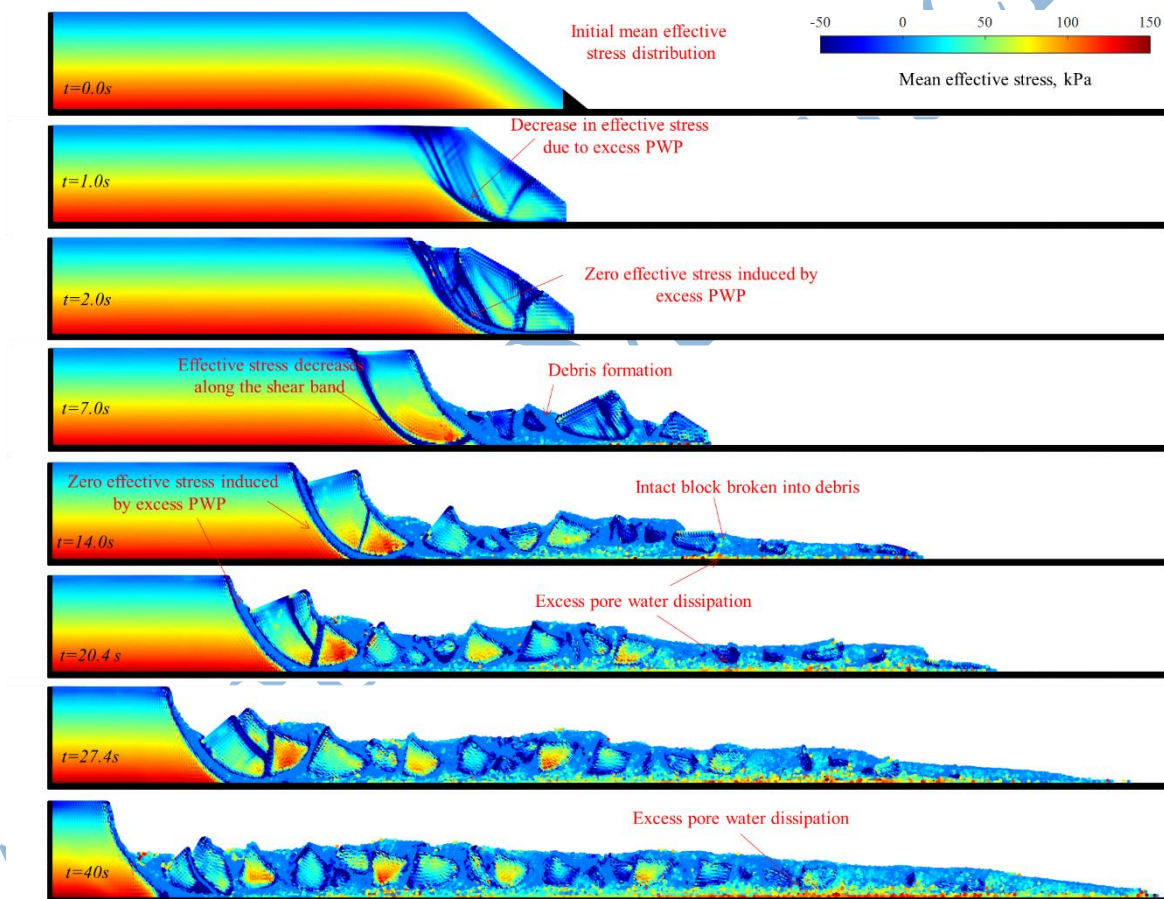


Fig. 21 Stabilised SPH modelling the evolution of mean effective stress in the flow retrogressive failure of sensitive clay slope with $K_0 = 0.5$.

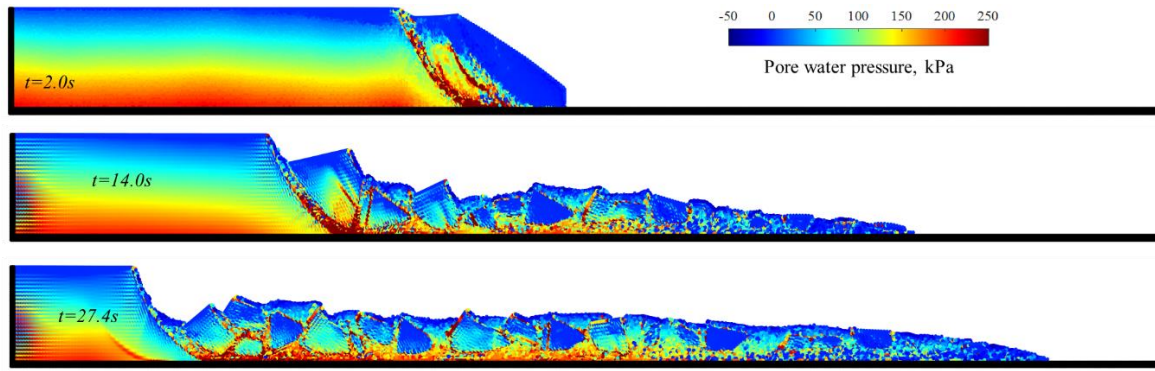


Fig. 22 Non-stabilised SPH prediction of the pore water pressure induced by contraction in the retrogressive failure of sensitive clay slope with $K_0 = 0.5$.

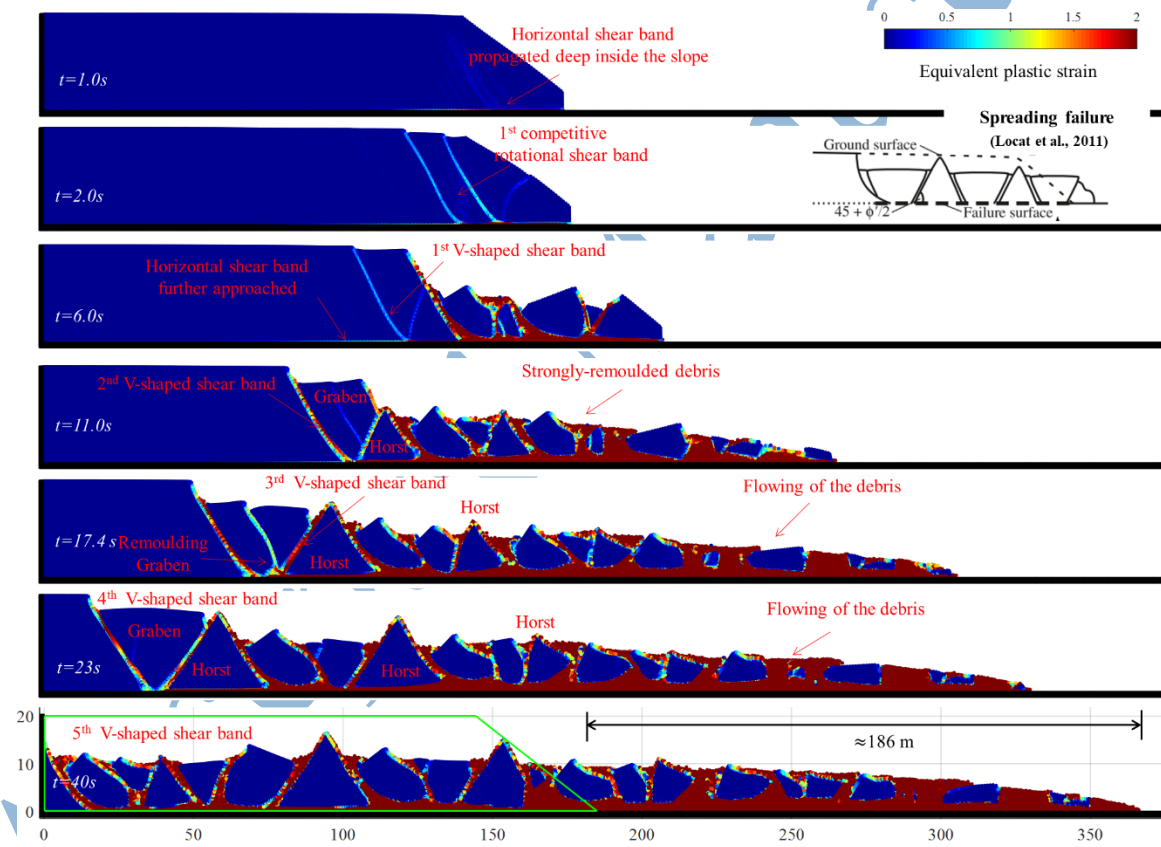


Fig. 23 Stabilised SPH modelling the spreading retrogressive failure of sensitive clay slope with $K_0 = 1.5$.

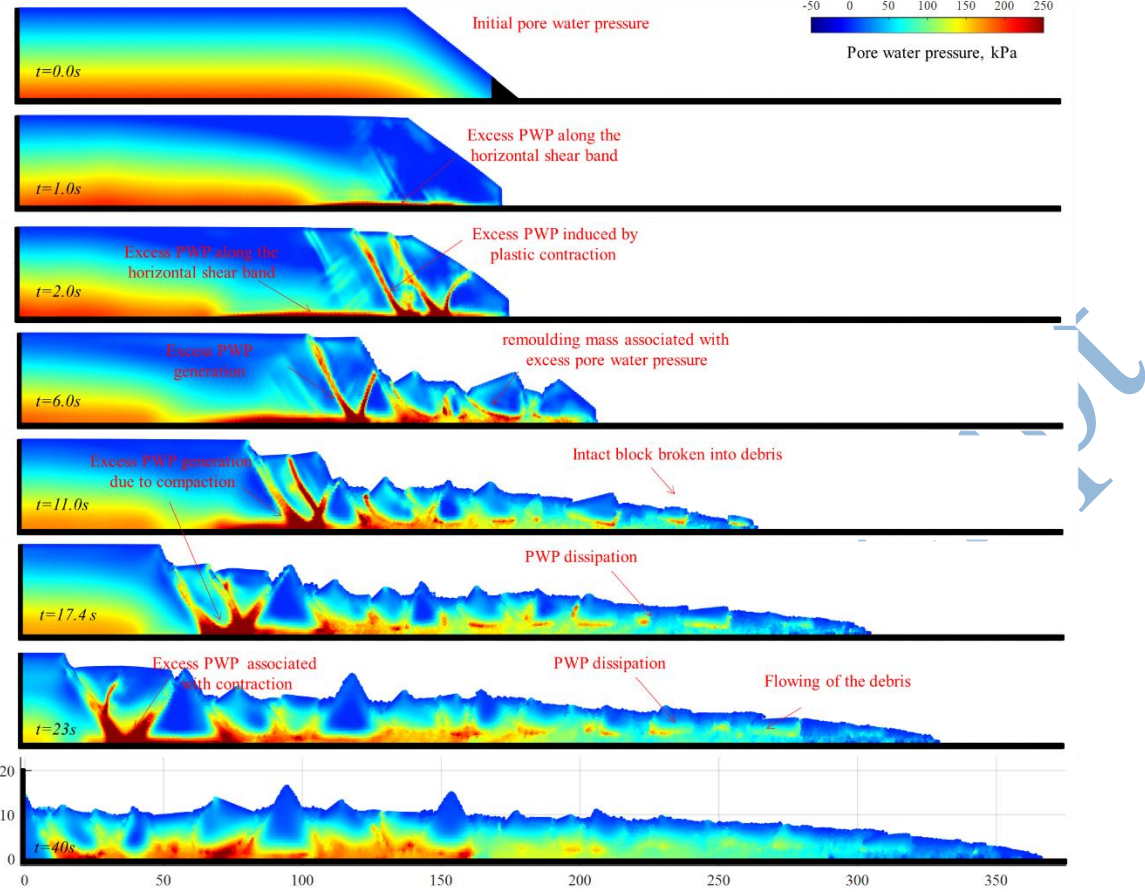


Fig. 24 The evolution of excess pore-water pressure induced by volumetric contraction in the spreading retrogressive failure of sensitive clay slope with $K_0 = 1.5$ predicted by the stabilised SPH model.

Figures 23-25 show the progressive failure of the slope predicted by the proposed SPH model with the lateral earth pressure coefficient of 1.5. A different failure process, namely spreading failure, is observed in this case. Unlike the first case, a horizontal shear band first develops and propagates inward the slope after removing the erodible soil block. This is because a larger value of K_0 , in this case, is associated with more reduction of the lateral stress in the back scarp soils when the slope toe is eroded [79]. More loss in the lateral stress to the back scarp then leads to the deeply-propagated horizontal shear band that triggers the spreading failure [70]. In this process, the very first curved failure plane with two competitive shear bands takes place at $t = 2\text{ s}$. This result is consistent with the conclusion reported by Odenstad (1951) [82], who pointed out that a circular slide could have first triggered the spreading failure. Competitive shear bands exist at the earlier failure stage due to the more lateral stress reduction in the back scarp soil [83]. As the first sliding block flowed out of the crater, the horizontal shear band at the level of the bottom continuously propagated deep inside the remaining slope at $t = 6.0\text{ s}$,

which then activated the 1st “V-shaped” failure surface that dislocated the sliding mass into a “Δ-shaped” horst and a “∇-shaped” grabens along with the horizontal shear band, as shown in Figure 23.

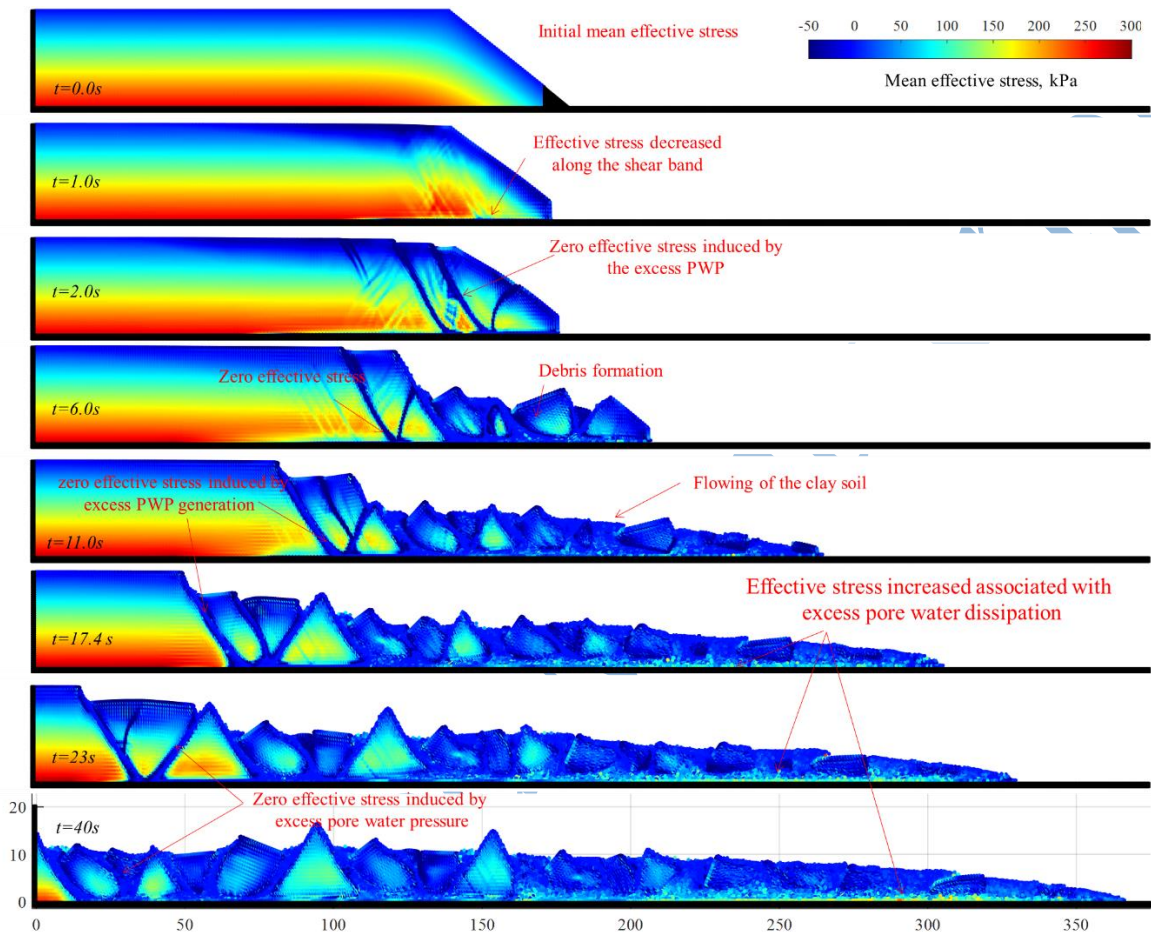


Fig. 25 Stabilised SPH prediction of the evolution of effective stress in the spreading retrogressive failure of sensitive clay slope with $K_0 = 1.5$.

Again, during the failure process, high excess pore-water pressure is also generated within the shear band due to the plastic volumetric contraction (see Figure 24), which strongly softens the shear strength of the materials (i.e., zero effective stress is observed in Figure 25), facilitating the rapid movement of the soil mass. The subsidence of the graben is intensively-remoulded at the bottom associated with intense excess pore-water pressure built-up, leaving an unstable slope face that can be pushed down the slope by another graben upslope, and forming another horst, thus the succession of horsts and graben in the scarp is triggered, i.e., at $t = 11$ s, 17.4 s and 23 s. This failure process continues along with the horizontal failure surface at the bottom

level until a stable back scarp is reached. The final run-out distance at $t = 40s$ is up to about 186 meters in this case. Moreover, it is noted that the predicted spreading failure of sensitive clay slope is close to the conceptual modelling results [70], as shown in Figure 23.

Figure 26 shows a qualitative comparison between the proposed SPH model, conceptional model and field observations for the formation of horst and graben [70,72]. The predicted results in this study are close to the reference results. For example, the proposed method captured well the remoulded soil at the base of grabens squeezing out of the cracks between grabens and horsts [72]. Moreover, the proposed model also captures the well-shape and intact horsts with a sharp wedge pointing upward. More importantly, the predicted angle of the sliding surface between grabens and horsts is around $45^\circ + \phi_p'/2$, which is close to the result given in [72]. Overall, the above modelling examples demonstrate that the proposed fully coupled SPH framework has a powerful capability in handling complex and large-scale coupled flow-deformation problems involving large deformation and post-failure processes.

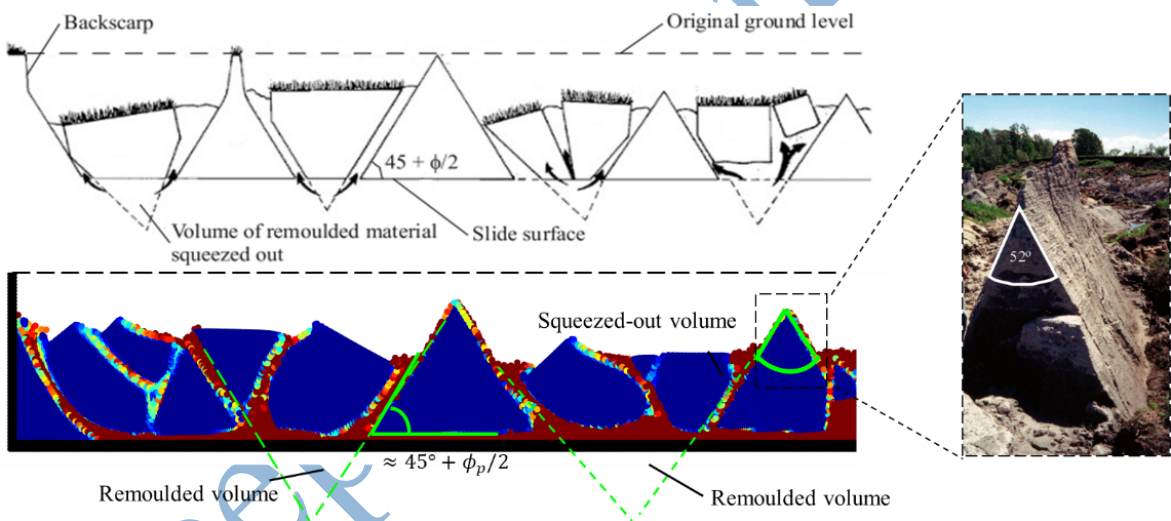


Fig. 26 SPH modelling the retrogressive flow failure of sensitive clay slope with $K_0 = 1.5$
(Reference result after [72]; Field photos after Locat et al.,[70])

5. CONCLUSION

This paper presents an effective and stabilised SPH computational framework for solving fully coupled flow-deformation problems in saturated porous media undergoing large deformations and failures. The newly proposed time integration scheme enables a larger timestep size for integrating the governing equation of the fluid phase, thus providing a more computationally efficient tool for field-scale applications. Compared with the existing fully explicit time integration scheme, the paper demonstrates that the proposed method helps save computational

costs (i.e., potentially up to 5~15 times in this study) when solving coupled flow-deformation problems, particularly for saturated porous media with large water bulk modulus or high permeability. Furthermore, the proposed stabilisation procedures help to obtain a stable solution for the fluid pressure field in saturated porous media when large deformation and post-failure behaviour are considered. The newly developed SPH framework enables the prediction of several challenging problems that were not achieved in the past. For example, to the best of the authors' knowledge, this is the first time the fully coupled analysis of the retrogressive failure of sensitive clay has been achieved. Compared to the commonly adopted "undrained" analysis, the current SPH model can capture the entire process of excess pore-water pressure development and dissipation during the post-failure process, thus offering an excellent way to have further insights into the failure mechanisms of sensitive clays. To this end, it is suggested that the proposed coupled SPH framework could be considered a useful computational tool to deal with a wide range of coupled flow-deformation problems in saturated porous media, particularly those involving large deformation and post-failure processes. However, additional work is required to adequately describe the localisation and shear band evolution processes, including bifurcation conditions to initiate localised failure and its associated shear band orientation and thickness. Such considerations, recently shown in [26-29] for fracturing applications, are in progress for soils and will be reported in the future.

Acknowledgement

The authors gratefully acknowledge support from the Australian Research Council via Discovery Projects DP170103793 (Nguyen, Bui), DP190102779 (Bui & Nguyen) and FT200100884 (Bui). Part of this research was undertaken with the assistance of resources and services from the National Computational Infrastructure (NCI), supported by the Australian Government. The support of the China Scholarship Council (CSC, No. 201906050025) is also gratefully acknowledged.

Reference

- [1] H.H. Bui, G.D. Nguyen, A coupled fluid-solid SPH approach to modelling flow through deformable porous media, *Int. J. Solids Struct.* 125 (2017) 244–264.
<https://doi.org/10.1016/j.ijsolstr.2017.06.022>.
- [2] S. Bandara, K. Soga, Coupling of soil deformation and pore fluid flow using material point method, *Comput. Geotech.* 63 (2015) 199–214.

<https://doi.org/10.1016/j.comgeo.2014.09.009>.

- [3] H.H. Bui, G.D. Nguyen, Smoothed particle hydrodynamics (SPH) and its applications in geomechanics: From solid fracture to granular behaviour and multiphase flows in porous media, *Comput. Geotech.* 138 (2021) 104315.
<https://doi.org/10.1016/j.comgeo.2021.104315>.
- [4] H. Sabetamal, M. Nazem, J.P. Carter, S.W. Sloan, Large deformation dynamic analysis of saturated porous media with applications to penetration problems, *Comput. Geotech.* 55 (2014) 117–131. <https://doi.org/10.1016/j.comgeo.2013.08.005>.
- [5] L. Monforte, M. Arroyo, J.M. Carbonell, A. Gens, Numerical simulation of undrained insertion problems in geotechnical engineering with the Particle Finite Element Method (PFEM), *Comput. Geotech.* 82 (2017) 144–156.
<https://doi.org/10.1016/j.comgeo.2016.08.013>.
- [6] Y.F. Jin, W.H. Yuan, Z.Y. Yin, Y.M. Cheng, An edge-based strain smoothing particle finite element method for large deformation problems in geotechnical engineering, *Int. J. Numer. Anal. Methods Geomech.* 44 (2020) 923–941.
<https://doi.org/10.1002/NAG.3016>.
- [7] E. Oñate, S.R. Idelsohn, F. Del Pin, R. Aubry, the Particle Finite Element Method — an Overview, *Int. J. Comput. Methods.* 01 (2004) 267–307.
<https://doi.org/10.1142/s0219876204000204>.
- [8] W.H. Yuan, J.X. Zhu, K. Liu, W. Zhang, B.B. Dai, Y. Wang, Dynamic analysis of large deformation problems in saturated porous media by smoothed particle finite element method, *Comput. Methods Appl. Mech. Eng.* 392 (2022) 114724.
<https://doi.org/10.1016/j.cma.2022.114724>.
- [9] L.B. Lucy, A numerical approach to the testing of the fission hypothesis, 82 (1977) 1013–1024.
- [10] A.R. Gingold, J.J. Monaghan, Smoothed particle hydrodynamics: theory and application to non-spherical stars, 181 (1977) 375–389.
- [11] H.H. Bui, R. Fukagawa, K. Sako, S. Ohno, Lagrangian meshfree particles method (SPH) for large deformation and failure flows of geomaterial using elastic–plastic soil constitutive model, *Int. J. Numer. Anal. Methods Geomech.* 32 (2008) 1537–1570.
<https://doi.org/10.1002/nag>.

- [12] A.H. Fávero Neto, R.I. Borja, Continuum hydrodynamics of dry granular flows employing multiplicative elastoplasticity, *Acta Geotech.* 13 (2018) 1027–1040. <https://doi.org/10.1007/s11440-018-0700-3>.
- [13] C.M. Chalk, M. Pastor, J. Peakall, D.J. Borman, P.A. Sleigh, W. Murphy, Stress-Particle Smoothed Particle Hydrodynamics : An application to the failure and post-failure behaviour of slopes, *Comput. Methods Appl. Mech. Eng.* 366 (2020) 113034. <https://doi.org/10.1016/j.cma.2020.113034>.
- [14] C.T. Nguyen, C.T. Nguyen, H.H. Bui, G.D. Nguyen, R. Fukagawa, A new SPH-based approach to simulation of granular flows using viscous damping and stress regularisation, *Landslides*. 14 (2017) 69–81. <https://doi.org/10.1007/s10346-016-0681-y>.
- [15] E. Yang, H.H. Bui, H. De Sterck, G.D. Nguyen, A. Bouazza, A scalable parallel computing SPH framework for predictions of geophysical granular flows, *Comput. Geotech.* 121 (2020) 103474. <https://doi.org/10.1016/j.compgeo.2020.103474>.
- [16] H.H. Bui, R. Fukagawa, K. Sako, J.C. Wells, Slope stability analysis and discontinuous slope failure simulation by elasto-plastic smoothed particle hydrodynamics (SPH), *Geotechnique*. 61 (2011) 565–574. <https://doi.org/10.1680/geot.9.P.046>.
- [17] X. He, D. Liang, M.D. Bolton, Run-out of cut-slope landslides: Mesh-free simulations, *Geotechnique*. 68 (2018) 50–63. <https://doi.org/10.1680/jgeot.16.P.221>.
- [18] H.H. Bui, R. Fukagawa, An improved SPH method for saturated soils and its application to investigate the mechanisms of embankment failure: Case of hydrostatic pore-water pressure, *Int. J. Numer. Anal. Methods Geomech.* 37 (2013) 31–50. <https://doi.org/10.1002/nag.1084>.
- [19] M. Pastor, T. Blanc, B. Haddad, S. Petrone, M. Sanchez Morles, V. Drempetic, D. Issler, G.B. Crosta, L. Cascini, G. Sorbino, S. Cuomo, Application of a SPH depth-integrated model to landslide run-out analysis, *Landslides*. 11 (2014) 793–812. <https://doi.org/10.1007/s10346-014-0484-y>.
- [20] T. Blanc, M. Pastor, A stabilized runge-kutta, taylor smoothed particle hydrodynamics algorithm for large deformation problems in dynamics, *Int. J. Numer. Methods Eng.* 91 (2012) 1427–1458. <https://doi.org/10.1002/nme.4324>.

- [21] S. Zhao, H.H. Bui, V. Lemiale, G.D. Nguyen, F. Darve, A generic approach to modelling flexible confined boundary conditions in SPH and its application, *Int. J. Numer. Anal. Methods Geomech.* 43 (2019) 1005–1031.
<https://doi.org/10.1002/nag.2918>.
- [22] E. Yang, H.H. Bui, G.D. Nguyen, C.E. Choi, C.W.W. Ng, H. De Sterck, A. Bouazza, Numerical investigation of the mechanism of granular flow impact on rigid control structures, *Acta Geotech.* (2021). <https://doi.org/10.1007/s11440-021-01162-4>.
- [23] B. Sheikh, T. Qiu, A. Ahmadipur, Comparison of SPH boundary approaches in simulating frictional soil–structure interaction, *Acta Geotech.* (2020) 1–20.
<https://doi.org/10.1007/s11440-020-01063-y>.
- [24] H.H. Bui, J.K. Kodikara, A. Bouazza, A. Haque, P.G. Ranjith, A novel computational approach for large deformation and post-failure analyses of segmental retaining wall systems, *Int. J. Numer. Anal. Methods Geomech.* 38 (2014) 1321–1340.
<https://doi.org/10.1002/nag.2253>.
- [25] D.S. Morikawa, M. Asai, Coupling total Lagrangian SPH–EISPH for fluid–structure interaction with large deformed hyperelastic solid bodies, *Comput. Methods Appl. Mech. Eng.* 381 (2021) 113832. <https://doi.org/10.1016/j.cma.2021.113832>.
- [26] H.T. Tran, Y. Wang, G.D. Nguyen, J. Kodikara, M. Sanchez, H.H. Bui, Modelling 3D desiccation cracking in clayey soils using a size-dependent SPH computational approach, *Comput. Geotech.* 116 (2019) 103209.
<https://doi.org/10.1016/j.comgeo.2019.103209>.
- [27] H.T. Tran, N.H.T. Nguyen, G.D. Nguyen, H.H. Bui, Meshfree SPH modelling of shrinkage induced cracking in clayey soils, *Lect. Notes Civ. Eng.* 54 (2020) 889–894.
https://doi.org/10.1007/978-981-15-0802-8_142.
- [28] Y. Wang, H.T. Tran, G.D. Nguyen, P.G. Ranjith, H.H. Bui, Simulation of mixed-mode fracture using SPH particles with an embedded fracture process zone, *Int. J. Numer. Anal. Methods Geomech.* 44 (2020) 1417–1445. <https://doi.org/10.1002/nag.3069>.
- [29] Y. Wang, H.H. Bui, G.D. Nguyen, P.G. Ranjith, A new SPH-based continuum framework with an embedded fracture process zone for modelling rock fracture, *Int. J. Solids Struct.* 159 (2019) 40–57. <https://doi.org/10.1016/j.ijsolstr.2018.09.019>.
- [30] S. Gharehdash, L. Shen, Y. Gan, Numerical study on mechanical and hydraulic

- behaviour of blast-induced fractured rock, *Eng. Comput.* 36 (2020) 915–929.
<https://doi.org/10.1007/s00366-019-00740-1>.
- [31] H.H. Bui, K. Sako, R. Fukagawa, Numerical simulation of soil-water interaction using smoothed particle hydrodynamics (SPH) method, *J. Terramechanics*. 44 (2007) 339–346. <https://doi.org/10.1016/j.jterra.2007.10.003>.
- [32] H.H. Bui, Lagrangian Mesh-free Particle Method (SPH) for Large Deformation and Post-failure of Geomaterial using Elasto-plastic Constitutive Models, Ritsumeikan Univ. (2006) Doctoral dissertation. http://rcube.ritsumei.ac.jp/repo/repository/rcube/9152/k_466_e.htm.
- [33] K. Maeda, H. Sakai, M. Sakai, Development of seepage failure analysis method of ground with Smoothed Particle Hydrodynamics, *Struct. Eng. / Earthq. Eng.* 23 (2006) 307s-319s. <https://doi.org/10.2208/JSCSEEEE.23.307S>.
- [34] H.H. Bui, R. Fukagawa, A first attempt to solve soil water coupled problems by SPH, *Japanese Terramech.* 29 (2008) 30–38.
- [35] M. Pastor, B. Haddad, G. Sorbino, S. Cuomo, V. Drempetic, A depth-integrated, coupled SPH model for flow-like landslides and related phenomena, *Int. J. Numer. Anal. Methods Geomech.* 33 (2009) 143–172. <https://doi.org/10.1002/NAG.705>.
- [36] Y. Lian, H.H. Bui, G.D. Nguyen, H.T. Tran, A. Haque, A general SPH framework for transient seepage flows through unsaturated porous media considering anisotropic features of diffusion, *Comput. Methods Appl. Mech. Eng.* 387 (2021) 114169. <https://doi.org/10.1016/j.cma.2021.114169>.
- [37] Y. Lian, H.H. Bui, G.D. Nguyen, S. Zhao, A. Haque, A computationally efficient SPH framework for unsaturated soils and its application to predicting the entire rainfall-induced slope failure process, *Géotechnique*. (2022) 1–60. <https://doi.org/10.1680/jgeot.21.00349>.
- [38] D.S. Morikawa, M. Asai, Soil-water strong coupled ISPH based on u-w-p formulation for large deformation problems, *Comput. Geotech.* 142 (2022) 104570. <https://doi.org/10.1016/j.comgeo.2021.104570>.
- [39] G. Ma, H.H. Bui, Y. Lian, K.M. Tran, G.D. Nguyen, A five-phase approach, SPH framework and applications for predictions of seepage-induced internal erosion and failure in unsaturated/saturated porous media, *Comput. Methods Appl. Mech. Eng.* 401

(2022) 115614. <https://doi.org/10.1016/j.cma.2022.115614>.

- [40] F. Brezzi, On the existence, uniqueness and approximation of saddle-point problems arising from Lagrangian multipliers, *Rev. Française d'Automatique Inform. Rech. Oper.* 8 (1974) 129–151.
- [41] M. Huang, Z.Q. Yue, L.G. Tham, O.C. Zienkiewicz, On the stable finite element procedures for dynamic problems of saturated porous media, *Int. J. Numer. Methods Eng.* 61 (2004) 1421–1450. <https://doi.org/10.1002/nme.1115>.
- [42] S. Kularathna, W. Liang, T. Zhao, B. Chandra, J. Zhao, K. Soga, A semi-implicit material point method based on fractional-step method for saturated soil, *Int. J. Numer. Anal. Methods Geomech.* 45 (2021) 1405–1436. <https://doi.org/10.1002/nag.3207>.
- [43] D. Mašín, C. Tamagnini, G. Viggiani, D. Costanzo, Directional response of a reconstituted fine-grained soil - Part II : Performance of different constitutive models, *Int. J. Numer. Anal. Methods Geomech.* 30 (2006) 1303–1336.
<https://doi.org/10.1002/nag>.
- [44] T. Blanc, M. Pastor, A stabilized Fractional Step, Runge-Kutta Taylor SPH algorithm for coupled problems in geomechanics, *Comput. Methods Appl. Mech. Eng.* 221–222 (2012) 41–53. <https://doi.org/10.1016/j.cma.2012.02.006>.
- [45] Y.F. Jin, Z.Y. Yin, Two-phase PFEM with stable nodal integration for large deformation hydromechanical coupled geotechnical problems, *Comput. Methods Appl. Mech. Eng.* 392 (2022) 114660. <https://doi.org/10.1016/j.cma.2022.114660>.
- [46] O.C. Zienkiewicz, A.H.C. Chan, M. Pastor, B.A. Schrefler, T. Shiomi, Computational geomechanics, Wiley, Chichester, 1999. [https://doi.org/10.1016/0148-9062\(96\)84010-1](https://doi.org/10.1016/0148-9062(96)84010-1).
- [47] F. Oka, B. Shahbodagh, S. Kimoto, A computational model for dynamic strain localization in unsaturated elasto-viscoplastic soils, *Int. J. Numer. Anal. Methods Geomech.* 43 (2019) 138–165. <https://doi.org/10.1002/nag.2857>.
- [48] P. Navas, L. Sanavia, S. López-Querol, R.C. Yu, U-W Formulation for Dynamic Problems in Large Deformation Regime Solved Through an Implicit Meshfree Scheme, *Comput. Mech.* 62 (2018) 745–760. <https://doi.org/10.1007/s00466-017-1524-y>.
- [49] P. Navas, M. Molinos, M.M. Stickle, D. Manzanal, A. Yagüe, M. Pastor, Explicit

- meshfree u- pw solution of the dynamic Biot formulation at large strain, *Comput. Part. Mech.* (2021). <https://doi.org/10.1007/s40571-021-00436-8>.
- [50] F. Zabala, E.E. Alonso, Progressive failure of aznalcó llar dam using the material point method, *Geotechnique*. 61 (2011) 795–808. <https://doi.org/10.1680/geot.9.P.134>.
- [51] A. Yerro, E.E. Alonso, N.M. Pinyol, The material point method for unsaturated soils, *Geotechnique*. 65 (2015) 201–217. <https://doi.org/10.1680/geot.14.P.163>.
- [52] J.J. Monaghan, Extrapolating B splines for interpolation, *J. Comput. Phys.* 60 (1985) 253–262. [https://doi.org/10.1016/0021-9991\(85\)90006-3](https://doi.org/10.1016/0021-9991(85)90006-3).
- [53] G. Oger, M. Doring, B. Alessandrini, P. Ferrant, An improved SPH method: Towards higher order convergence, *J. Comput. Phys.* 225 (2007) 1472–1492. <https://doi.org/10.1016/j.jcp.2007.01.039>.
- [54] P.W. Randles, L.D. Libersky, Smoothed particle hydrodynamics: Some recent improvements and applications, *Comput. Methods Appl. Mech. Eng.* 139 (1996) 375–408. [https://doi.org/10.1016/S0045-7825\(96\)01090-0](https://doi.org/10.1016/S0045-7825(96)01090-0).
- [55] P.W. Cleary, J.J. Monaghan, Conduction Modelling Using Smoothed Particle Hydrodynamics, *J. Comput. Phys.* 148 (1999) 227–264. <https://doi.org/10.1006/jcph.1998.6118>.
- [56] P. Español, M. Revenga, Smoothed dissipative particle dynamics, *Phys. Rev. E - Stat. Physics, Plasmas, Fluids, Relat. Interdiscip. Top.* 67 (2003) 12. <https://doi.org/10.1103/PhysRevE.67.026705>.
- [57] H.H. Bui, R. Fukagawa, K. Sako, J.C. Wells, Slope stability analysis and discontinuous slope failure simulation by elasto-plastic smoothed particle hydrodynamics (SPH), *Geotechnique*. 61 (2011) 565–574. <https://doi.org/10.1680/geot.9.P.046>.
- [58] H.H. Bui, R. Fukagawa, An improved SPH method for saturated soils and its application to investigate the mechanisms of embankment failure: Case of hydrostatic pore-water pressure, *Int. J. Numer. Anal. Methods Geomech.* 30 (2011) 1303–1336. <https://doi.org/10.1002/nag>.
- [59] S. Shao, E.Y.M. Lo, Incompressible SPH method for simulating Newtonian and non-Newtonian flows with a free surface, *Adv. Water Resour.* 26 (2003) 787–800. [https://doi.org/10.1016/S0309-1708\(03\)00030-7](https://doi.org/10.1016/S0309-1708(03)00030-7).

- [60] Nomeritae, E. Daly, S. Grimaldi, H.H. Bui, Explicit incompressible SPH algorithm for free-surface flow modelling: A comparison with weakly compressible schemes, *Adv. Water Resour.* 97 (2016) 156–167. <https://doi.org/10.1016/j.advwatres.2016.09.008>.
- [61] D.A. Barcarolo, Improvement of the precision and the efficiency of the SPH method : theoretical and numerical study, *Fluids Mech. [Physics.Class-Ph]. Ec. Cent. Nantes.* (2013).
- [62] M. Hopp-Hirschler, U. Nieken, Fully implicit time integration in truly incompressible SPH, *Eur. Phys. J. Spec. Top.* 227 (2019) 1501–1514. <https://doi.org/10.1140/epjst/e2019-800152-6>.
- [63] H.H. Bui, R. Fukagawa, An improved SPH method for saturated soils and its application to investigate the mechanisms of embankment failure: Case of hydrostatic pore-water pressure, *Int. J. Numer. Anal. Methods Geomech.* 37 (2013) 31–50. <https://doi.org/10.1002/NAG.1084>.
- [64] O.C. Zienkiewicz, C.T. Chang, P. Bettess, Drained, undrained, consolidating and dynamic behaviour assumptions in soils, *Geotechnique.* 30 (1980) 385–395. <https://doi.org/10.1680/geot.1980.30.4.385>.
- [65] R. de Boer, W. Ehlers, Z. Liu, One-dimensional transient wave propagation in fluid-saturated incompressible porous media, *Arch. Appl. Mech.* 63 (1993) 59–72. <https://doi.org/10.1007/BF00787910>.
- [66] H. Sabetamal, M. Nazem, S.W. Sloan, J.P. Carter, Frictionless contact formulation for dynamic analysis of nonlinear saturated porous media based on the mortar method, *Int. J. Numer. Anal. Methods Geomech.* 40 (2016) 25–61. <https://doi.org/10.1002/nag.2386>.
- [67] P. Navas, M. Pastor, A. Yagüe, M.M. Stickle, D. Manzanal, M. Molinos, Fluid stabilization of the u–w Biot’s formulation at large strain, *Int. J. Numer. Anal. Methods Geomech.* 45 (2021) 336–352. <https://doi.org/10.1002/nag.3158>.
- [68] Abaqus 6.11 Theory manual, (n.d.).
- [69] N. Manoharan, S.P. Dasgupta, Consolidation analysis of elasto-plastic soil, *Comput. Struct.* 54 (1995) 1005–1021. [https://doi.org/10.1016/0045-7949\(94\)00403-P](https://doi.org/10.1016/0045-7949(94)00403-P).
- [70] A. Locat, S. Leroueil, S. Bernander, D. Demers, H.P. Jostad, L. Ouehb, Progressive failures in eastern canadian and scandinavian sensitive clays, *Can. Geotech. J.* 48

(2011) 1696–1712. <https://doi.org/10.1139/t11-059>.

- [71] D.M. Cruden, D.J. Varnes, Chapter 3 Landslide Types and Processes, *Landslides Investig. Mitigation, Transp. Res. Board Spec. Rep.* 247, Washingt. D.C. (1996) 36–75.
- [72] M.A. Carson, On the retrogression of landslides in sensitive muddy sediments, *Can. Geotech. J.* 14 (1977) 582–602. <https://doi.org/10.1139/t77-059>.
- [73] S. Bernander, *Progressive Landslides in Long Natural Slopes*, Luleå University of Technology, Luleå, Sweden, 2011.
- [74] R. Dey, B. Hawlader, R. Phillips, K. Soga, Numerical modeling of combined effects of upward and downward propagation of shear bands on stability of slopes with sensitive clay, *Int. J. Numer. Anal. Methods Geomech.* 40 (2016) 2076–2099. <https://doi.org/10.1002/nag.2522>.
- [75] X. Zhang, S.W. Sloan, E. Oñate, Dynamic modelling of retrogressive landslides with emphasis on the role of clay sensitivity, *Int. J. Numer. Anal. Methods Geomech.* 42 (2018) 1806–1822. <https://doi.org/10.1002/nag.2815>.
- [76] B. Wang, P.J. Vardon, M.A. Hicks, Investigation of retrogressive and progressive slope failure mechanisms using the material point method, *Comput. Geotech.* 78 (2016) 88–98. <https://doi.org/10.1016/j.compgeo.2016.04.016>.
- [77] Y.F. Jin, Z.Y. Yin, W.H. Yuan, Simulating retrogressive slope failure using two different smoothed particle finite element methods: A comparative study, *Eng. Geol.* 279 (2020) 105870. <https://doi.org/10.1016/j.enggeo.2020.105870>.
- [78] W.H. Yuan, K. Liu, W. Zhang, B. Dai, Y. Wang, Dynamic modeling of large deformation slope failure using smoothed particle finite element method, *Landslides*. 17 (2020) 1591–1603. <https://doi.org/10.1007/s10346-020-01375-w>.
- [79] C. Wang, B. Hawlader, D. Perret, K. Soga, J. Chen, Modeling of Initial Stresses and Seepage for Large Deformation Finite-Element Simulation of Sensitive Clay Landslides, *J. Geotech. Geoenvironmental Eng.* 147 (2021) 04021111. [https://doi.org/10.1061/\(asce\)gt.1943-5606.0002626](https://doi.org/10.1061/(asce)gt.1943-5606.0002626).
- [80] F. Tremblay-Auger, A. Locat, S. Leroueil, P. Locat, D. Demers, J. Therrien, R. Mompin, The 2016 landslide at saint-luc-de-vincennes, quebec: Geotechnical and morphological analysis of a combined flowslide and spread, *Can. Geotech. J.* 58

(2021) 295–304. <https://doi.org/10.1139/cgj-2019-0671>.

- [81] K.K. Hamouche, S. Leroueil, M. Roy, A.J. Lutenegger, In situ evaluation of K₀ in eastern Canada clays, *Can. Geotech. J.* 32 (1995) 677–688. <https://doi.org/10.1139/t95-067>.
- [82] S. Odenstad, The landslide in Skoptrop on the Lidan river, R. Swedish Geotech. Inst. Proc. No. 4. (1951).
- [83] D.M. Potts, N. Kovacevlc, P.R. Vaughan, Delayed collapse of cut slopes in stiff clay, *Geotechnique*. 47 (1997) 953–982. <https://doi.org/10.1680/geot.1997.47.5.953>.